Seismically-induced serpentine dehydration as a possible mechanism of water release in subduction zones. Insights from the Alpine Corsica pseudotachylyte-bearing Monte Maggiore ophiolitic unit

Remi Magott, Olivier Fabbri, Marc Fournier

To cite this version:

Remi Magott, Olivier Fabbri, Marc Fournier. Seismically-induced serpentine dehydration as a possible mechanism of water release in subduction zones. Insights from the Alpine Corsica pseudotachylyte-bearing Monte Maggiore ophiolitic unit. Lithos, 2020, 362-363, pp.105474. 10.1016/j.lithos.2020.105474 . hal-02560403

HAL Id: hal-02560403
https://hal.science/hal-02560403v1

Seismically-induced serpentine dehydration as a possible mechanism of water release in subduction zones. Insights from the Alpine Corsica pseudotachylyte-bearing Monte Maggiore ophiolitic unit

Rémi Magott [1-2]*, Olivier Fabbri [2] and Marc Fournier [3]

1 : CRPG, UMR CNRS 7358, Université de Lorraine, F-54501, Vandœuvre-lès-Nancy, France

2 : Laboratoire Chrono-environnement, UMR CNRS 6249, Univ. Bourgogne Franche-Comté, F-25000 Besançon, France

3 : Sorbonne Universités, UPMC Univ. Paris 06, UMR 7193, ISTEP, F-75005 Paris, France

* Corresponding author: remi.magott@gmail.com
CRPG, UMR CNRS 7358
15, rue Notre-Dame des Pauvres
54500 Vandoeuvre-lès-Nancy
FRANCE

HIGHLIGHTS

- Seismic rupture can propagate through serpentinized peridotite in subducting slabs at 20 to 30 km depths.
- Co-seismic frictional melting can locally dehydrate antigorite into olivine.
- Co-seismic dehydration appears as a possible source of water in subducting slabs.

ABSTRACT

The Monte Maggiore ophiolitic unit of Alpine Corsica consists of an intact to variably hydrated spinel lherzolite intruded by Jurassic gabbro dykes. A widespread serpentinization, marked by low-pressure serpentine polymorphs, results from sea water interaction with mantle rocks during Jurassic sea-floor spreading of the Piemonte-Liguria ocean. A second serpentinization event, marked by the presence of antigorite, is related to the Cretaceous to Paleogene subduction of the Piemonte-Liguria oceanic lithosphere. Tectonic pseudotachylyte veins locally, crosscutting the unit, display several original characteristics. (1) They are hosted by serpentinite, showing that seismic ruptures can propagate through hydrated mantle rocks. (2) The host serpentinite in contact with pseudotachylyte veins shows a thin (500 μm or less) rim of secondary olivine newly crystallized at the expense of serpentine. The heat necessary for serpentine dehydration is likely provided by the frictional melt. Antigorite-bearing clasts (themselves partly dehydrated along their boundaries) reworked in pseudotachylyte veins on one hand and antigorite veins crossing pseudotachylyte veins on the other hand show that frictional melting took place at pressure and temperature conditions compatible with antigorite stability. This indicates that frictional meting occurred at pressures between 0.7 and 0.85 GPa, that is, at ~20 to ~30 km depths in the subducting Piemonte-Liguria oceanic slab. Since the dehydration of serpentine into olivine is only observed at the host-rock selvages of pseudotachylyte veins, it cannot be related to the crossing, by the subducting slab, of the regional 610 ± 100 °C isotherm of the subduction zone, temperature at which antigorite starts to dehydrate into olivine. An estimate of the water released by the dehydration reaction suggests that for a magnitude 6 earthquake, the average amount is about 1.36 L/m^2 or 1.36 x 10^5 m^3 for the entire rupture surface (assumed to be 100 km^2). If the released water is not incorporated in the nearby frictional melt, it can flow away from the slip zone and contribute to the various fluid-rock interactions active in subduction zones. Alternatively, if the water cannot escape from the slip zone and if the pore pressure is locally high enough, it could trigger aftershocks following the initial seismic rupture.

KEYWORDS

Pseudotachylyte, peridotite, serpentinite, subduction, dehydration, olivine, antigorite, Corsica

1. Introduction.

Since the precursor works of Raleigh and Paterson (1965) and Rutter and Brodie (1988), serpentinite dehydration is regarded as a major mechanism to account for intermediate-depth seismicity (70 to 300 km depth, Frohlich, 2006) in subduction zones (Peacock, 2001; Dobson et al., 2002; Hacker et al., 2003; Yamasaki and Seno, 2003; Jung et al., 2004; Nakajima et al., 2009; Ferrand et al., 2017; Wang et al., 2017; Kita and Ferrand, 2018). More specifically, oceanic lithosphere formed along a slow-spreading ridge is expected to experience pervasive and widespread serpentinization. Once such a hydrated lithosphere is subducted at a depth where pressure and temperature conditions are high enough to allow dehydration reactions (Ulmer and Trommsdorff, 1995; Wunder and Schreyer, 1997; Schmidt and Poli, 1998; Guillot et al., 2015), serpentine dehydration can release water which in turn can lead to fault destabilization by decreasing the normal stress acting on fault surfaces (Houston, 2015). This mechanism is referred to as dehydration embrittlement.

In Alpine Corsica, ultramafic and mafic pseudotachylytes are reported from the Cima di Gratera (Austrheim and Andersen, 2004; Andersen and Austrheim, 2006; Andersen et al., 2008; 2014; Deseta et al., 2014; Magott et al., 2016; 2017) and Monte Maggiore ophiolitic units (Magott, 2016; Fabbri et al., 2018). Other reports of ultramafic and mafic pseudotachylytes in the Alpine orogen come from the Moncuni peridotite unit of the Lanzo massif in Italy (Piccardo et al., 2010; Scambelluri et al., 2017). The Cima di Gratera occurrence is interpreted as resulting from intermediate-depth seismicity during the subduction of the Piemonte-Liguria oceanic lithosphere. The Moncuni occurrences were initially interpreted as the result of mid-oceanic ridge faulting during oceanic extension (Piccardo et al., 2010). Based on eclogite facies metamorphic assemblages preserved in the veins, Scambelluri et al. (2017) show that the Lanzo occurrences are likely related to intermediate-depth seismicity in the subducting Piemonte-Liguria lithosphere. In both the Cima di Gratera and Lanzo occurrences, pseudotachylyte veins developed in a fresh (i.e., not serpentinized) peridotite. Conversely, in the Monte Maggiore, the pseudotachylyte veins cross-cut serpentinized peridotite, providing an opportunity to examine interactions between pseudotachylyte and serpentinite.

In this study, we describe evidence for dehydration of serpentinized peridotite by thermal metamorphism caused by tectonic pseudotachylyte. The presence of secondary olivine formed by dehydration of serpentine at the contact with pseudotachylyte veins shows that seismic ruptures can propagate through a hydrated peridotite. The preservation of antigorite, a high-pressure serpentine polymorph, further allows to estimate the depth of seismicity at the origin of the formation of pseudotachylyte. Lastly, the amount of water released by serpentine dehydration is estimated and the consequences of the water release in the subducting slab are discussed.

2. Geological setting.

In the northwestern end of the Cap Corse peninsula, the Monte Maggiore ultramafic unit consists of a peridotite-dominated ophiolitic thrust sheet belonging to the *Schistes Lustrés* Complex (Fig. 1). It is considered as a remnant of the oceanic lithosphere of the Piemonte-Liguria ocean opened by rifting and slow to ultra-slow spreading during Jurassic to early Cretaceous times (Ohnenstetter et al., 1981; Lagabrielle and Lemoine, 1997; Manatschal and Müntener, 2009; Rampone et al., 2009; Piccardo and Guarnieri, 2010). Mineralogical and geochemical characteristics of the peridotites of the Monte Maggiore unit are similar to those observed in other Alpine ophiolitic units and in present-day oceanic floor peridotite (Piccardo and Guarnieri, 2010; Rampone et al., 2009; Rampone and Hofmann, 2012).

The Monte Maggiore unit is composed of a spinel-plagioclase lherzolite along with clinopyroxene-depleted peridotite and minor dunite (Piccardo and Guarnieri, 2010). The texture is granoblastic. Where preserved, the original mineral assemblage is typical of a spinel lherzolite with olivine > clinopyroxene > orthopyroxene > spinel and minor plagioclase and chromite. Numerous decimeter- to meter-thick gabbroic dykes cross-cut the peridotite. Centimeter-scale chromite pods are also observed. The Monte Maggiore unit is thrust over gneisses of continental origin (Lahondère, 1992; Meresse et al., 2012). The ~~entire~~ Monte Maggiore peridotite is affected by a pervasive tectonic fabric associated with a top-to-the-west sense of shear. This fabric is related to a tectonic deformation during oceanic accretion (Jackson and Ohnenstetter, 1981). It is locally overprinted by an unevenly distributed cataclastic foliation (Fabbri et al., 2018).

The Monte Maggiore peridotite is variably serpentinized. Serpentinization is interpreted as the result of mantle hydration during the opening of the Piemonte-Liguria oceanic basin (Debret, 2013). Primary olivine and, to a lesser extent, pyroxene, are replaced by lizardite, magnetite and minor chrysotile, especially in the southern and the eastern parts of the Monte Maggiore unit (Debret, 2013; Fig. 1). The degree of serpentinization is higher near the tectonic contact with the Centuri gneiss unit (~ 100 %) and decreases northwards (~50 %). Some zones randomly distributed inside the unit are also significantly serpentinized (between 50 and 80 %, Debret, 2013; Fig. 1). Serpentinization appears diffuse throughout the peridotite or localized along veins which do not exceed 20 cm in length and 5 mm in thickness. Thin section observation shows that the diffuse serpentinization corresponds to what is referred to as mesh texture (Viti and Mellini, 1998; Rumori et al., 2004; Andréani et al., 2007). Serpentine veins are randomly oriented. Based on the cross-cutting relationships between diffuse serpentinization and serpentine veins, Debret (2013) distinguishes three stages of serpentinization. The first stage S1 consists of the isotropic development of lizardite and minor chrysotile associated to magnetite. The second stage S2 consists of the pervasive formation of lizardite and minor chrysotile in mesh texture and the partial substitution of pyroxene (both ortho- and clinopyroxene) by bastite. The development of fibrous lizardite veins is also frequent. Stage S2 serpentinization is the most widespread in the Monte Maggiore unit. The third stage S3 is characterized by the formation of lizardite crack-seal veins and by overgrows of lizardite and chrysotile along the walls of pre-existing lizardite veins. At the scale of the unit, each serpentinization event can be variably developed. All these events are characteristic of an intra-oceanic peridotite serpentinization (Mével, 2003; Andréani et al., 2007; Debret et al., 2013).

In addition to the three stages described by Debret (2013), a fourth stage of serpentinization S4 is observed in the central part of the Monte Maggiore unit, at localities 1 and 2 (Magott, 2016; Fabbri et al., 2018). This stage, characterized by the crystallization of antigorite, can be subdivided into two sub-stages. A sub-stage *S4a* corresponds to a diffuse metamorphic substitution of lizardite by antigorite. A sub-stage *S4b* corresponds to antigorite veins crossing all other structures. The vein-filling antigorite is fibrous~~,~~ and the fibers are perpendicular or highly oblique to the vein walls (Fig. 2). In some instances, several stages of opening can be distinguished (Fig. 2B), suggesting cyclic fluid input and vein opening (crack-seal opening mechanism).

The Monte Maggiore unit was affected by a greenschist facies condition metamorphism. In the peridotite, this metamorphic event is indicated by the partial substitution of pyroxene by tremolite + actinolite + minor chlorite and of olivine by tremolite + chlorite. In the metagabbro dykes, this event is responsible for hornblende overgrowths on primary pyroxene. This first greenschist facies condition event is followed by a blueschist facies condition event attested, in the metagabbro dykes, by the partial replacement of plagioclase by jadeite + zoisite + paragonite + chlorite assemblages (Jackson and Ohnenstetter, 1981; Nicollet et al., 2001). Primary clinopyroxene is commonly rimmed by glaucophane overgrowths. This medium- to high-pressure metamorphic event is interpreted as a consequence of the subduction of the Piemonte-Liguria oceanic lithosphere beneath a continental block or island arc (Nicollet et al., 2001; Molli, 2008; Molli and Malavieille, 2011; Vitale-Brovarone et al., 2013). According to the metagabbro mineralogical assemblages, the peak of metamorphism recorded by the Monte Maggiore unit is about 450°C and 0.85 GPa (Nicollet et al., 2001). A late retrograde greenschist metamorphic facies event tentatively associated with exhumation is evidenced in the metagabbro dykes by rare instances of green hornblende surrounding glaucophane overgrowths (Nicollet et al., 2001; Debret, 2013). The partial substitution of olivine by tremolite and chlorite assemblages is tentatively related to this late retrograde event.

In the central part of the Monte Maggiore unit (localities 1, 2 and 3, Fig. 1), the serpentinized peridotite is cross-cut by tectonic pseudotachylyte veins (Magott, 2016). Outcrop-scale, hand-sample scale and thin-section-scale petrographic and structural characteristics of the veins (Fig. 3) are similar to the Cima di Gratera pseudotachylyte occurrence. These similarities suggest that the Monte Maggiore pseudotachylyte occurrence could represent a possible extension of the fossil Wadati-Benioff seismogenic zone described in the Cima di Gratera unit located further south (Fabbri et al., 2018). A characteristic of the Monte Maggiore occurrence is that the formation of pseudotachylyte veins was polyphase, as indicated by numerous cross-cutting relationships between veins and also by the reworking of pseudotachylyte clasts in pseudotachylyte veins. Another characteristic of the Monte Maggiore pseudotachylyte occurrence, which is also observed in the Cima di Gratera occurrence, is that frictional melting occurred concurrently with cataclasis. Some hand sample sections and thin sections show pseudotachylyte fault veins cross-cutting cataclastic serpentinite (Fig. 4), whereas other hand sample sections or thin sections show that cataclasis post-dates frictional melting (Fabbri et al., 2018). In the latter case, cataclasis develops along the boundary between fault veins and the host rock. They form 0.5 to 2.5 cm thick, cataclastic layers which, at the hand sample-scale, look like pseudotachylyte fault veins (Fig. 3D). Thin section observation shows that the cataclastic layers contain clasts of pseudotachylyte and that some relict melted rock is preserved along the margin of the layers (Fabbri et al., 2018). These observations indicate that cataclastic layers developed at the expense of pre-existing fault veins. The cataclastic layers and the pseudotachylyte veins are parallel to the cataclastic foliation nearby, if any.

3. Material and methods

Polished thin sections were prepared from oriented samples of ultramafic pseudotachylyte and related host rocks. Thin sections were examined by optical and scanning electron microscopes. Scanning electron microscopy (SEM) was performed at CRPG (Vandœuvre-lès-Nancy, France) and FEMTO-ST (University of Bourgogne-Franche-Comté, Besançon, France). Primary mineral composition was determined with a CAMECA SX100 electron microprobe at the SCMEM, University of Lorraine, France. Analyses include bulk matrix (wide beam), wall-rock, non-melted minerals, crystallization products (microlites) as well as serpentinization-related minerals. The determination of serpentine polymorphs was done with RXN1 Raman spectroscopy at the Georessources laboratory (UMR 7359), University of Lorraine, France. Raman analyses were performed on serpentine polymorphs in the veins and on mesh structures in the host rock. Where serpentine veins are present, the analyses in the host rock were done at different distances to the vein to estimate the importance of serpentinization on both sides of the vein. Serpentine in pseudotachylyte matrix and clasts were also characterized by Raman spectroscopy.

4. Results.

4.1. Microscopic characteristics.

4.1.1. Microscopic characteristics of the serpentinized peridotite hosting the pseudotachylyte veins.

In localities 1 and 2 (Fig. 1), the serpentinized peridotite typically shows an assemblage of serpentine + magnetite + clinopyroxene + orthopyroxene ± rare relict olivine. The olivine site is partly or totally replaced by serpentine. The pyroxene site can be crossed by serpentine veins or can display a weakly developed serpentinization along cleavage planes. Pyroxene pseudomorphozed by serpentine (bastite) is locally observed.

4.1.2. Microscopic characteristics of pseudotachylyte

Where not serpentinized, pseudotachylyte veins are characterized by abundant spherulitic or acicular microlites embedded in a brownish ultrafine-grained or crypto-crystalline matrix (Fig. 4A, B and C, Fig. 5A and F). Polygonal textures suggest that a part of the matrix was glassy, before eventual devitrification. Microlite size ranges between 20 µm and 150 µm. The spatial density and the size of microlites varies from the median part of the vein to the margins (Fig. 5A and E). Vein margins are 80 to 200 mm thick and are characterized by a high density of tiny microlites (< 10µm, Fig. 5A). The central parts of the veins show an increase of the microlite size and an evolution of their crystalline shapes from dendritic or spherulitic shapes toward more mature shapes, especially lath shapes (Fig. 5A and E). The microlites consist of acicular or spherulitic clinopyroxene and subordinate olivine with lath shapes. Fault veins and to a lesser extent injection veins are characterized by variable proportions of clasts (*ca.* 10%). The clasts have sizes between 50 and 800 µm (mean value around 250 µm), are rounded, and consist of assemblages of olivine (commonly partly serpentinized) + serpentine ± pyroxene ± ilmenite (Fig. 4; Fig. 5A and C). Clasts of pseudotachylyte and of polycrystalline aggregates of olivine or pyroxene are also observed (Fig. 4B and Fig. 5D). Some clasts display embayments that are interpreted as corrosion textures (Fig. 5B). In fault veins, clasts close to the wall rock are frequently elongated parallel to the vein boundary. Conversely, the rounded clasts located in the median part of the veins are larger and rarely elongated. Ilmenite clasts are smaller than the clast derived from other minerals, with an average size around 10 µm. The small size of these microlites could be a consequence of a preferential melting of ilmenite which is a mineral characterized by a lower thermal shock resistance than olivine or pyroxene. Extreme comminution due to thermal shock fragmentation could have led to an almost total assimilation of the fragments by the melt, therefore impeding the growth of ilmenite microlites during melt cooling, as proposed by Papa et al. (2018) to account for the scarcity or the small size of garnets microlites in an amphibolite-facies pseudotachylyte occurrence from the western Alps.

In the vicinity of secant *S4b* serpentine veins, pseudotachylyte microlites are partly serpentinized (Fig. 3C). This serpentinization is characterized by vermicular to fibrous antigorite scattered in the ultrafine-grained or crypto-crystalline matrix or invading microlites and clasts (Fig. 5F). Since this serpentinization is observed next to *S4b* antigorite veins, it is interpreted as relevant to this stage.

4.2. Mineral chemistry and Raman data.

4.2.1. Mineral chemistry and Raman data of the serpentinized peridotite.

In the fresh (i.e., not serpentinized) peridotite, olivine is characterized by a homogeneous X_{Mg} value between 0.82 and 0.84 (Table 1; Piccardo and Guarnieri, 2010). Clinopyroxene composition is between augite and diopside, but augite composition predominates. Orthopyroxene shows an enstatite composition and includes noticeable amounts of FeO (6 wt.% FeO), Al_2O_3 (4 wt.% Al_2O_3) and minor traces of Cr_2O_3 (between 0.5 and 0.7 wt.% Cr_2O_3). The serpentinized peridotite consists of an assemblage of serpentine + magnetite + clinopyroxene + orthopyroxene ± rare olivine. In samples from localities 1 and 2, serpentine is mainly lizardite along with minor amounts of chrysotile, both being partly overprinted by antigorite (Fig. 6A). Stage S4 antigorite is characterized by a X_{Mg} value around 0.89, that is slightly higher than that of primary olivine (Table 1). According to Debret (2013), stage S1 serpentine phases are characterized by an Al_20_3 content between 0.5 and 1.0 wt.% and by a FeO content between 3.9 and 6.2 wt.%. The Raman spectra display peaks at 230, 345, 385, 465, 620, 687 and 1103 $^{cm-1}$ at low frequency and 3683 and 3705 cm^{-1} at high frequency (Debret, 2013). These peaks are typical of lizardite (Rinaudo and Gastaldi, 2003; Auzende et al., 2004; Groppo et al., 2006). The peak at 3695 cm^{-1} indicates the presence of chrysotile. Stage S2 serpentine phases are characterized by an Al_20_3 content between 0.2 and 2.2 wt% and by a FeO content between 2.8 and 7.8 wt%. The Raman spectra are similar to those of lizardite with characteristic peaks at 229, 383, 464, 617, 659 and 1100 cm^{-1} at low frequency and 3685 and 3704 cm^{-1} at high frequency. Weak peaks at 3695 cm^{-1} attest of the presence of small amounts of chrysotile (Debret, 2013). Stage S3 serpentine phases, which occur mainly under the form of veins, have an

Al_20_3 content between 1.6 to 2.1 wt.% and a Fe0 content between 4.5 to 5.5 wt.%. The Raman spectra are intermediate between lizardite and chrysotile spectra with peaks at 229, 383, 474, 620, 689, 1100 cm^{-1} at low frequency and at 3683, 3690 and 3704 cm^{-1} (Debret, 2013).

4.2.2. Mineral chemistry and Raman data of the pseudotachylyte.

The composition of the pseudotachylyte matrix is close to that of olivine, but includes significant amounts of Al_2O_3 (up to 6.5 wt.%), and minor amounts of CaO (between 2.91 and 3.72 wt.% CaO; Table 2). Cr_20_3, TiO_2 and NiO contents are slightly higher than in host rock primary minerals, with values around 0.15-0.29 wt.% Cr_2O_3, 0.2-0.3 wt.% TiO_2 and 0.08-0.12 wt.% NiO. The matrix also displays X_{Mg} values between 0.78 and 0.82. These values are close to those of primary olivine. The absence of plagioclase or orthopyroxene in the microlites or in survivor clasts while they are present in the host rock is due to the lower melting temperature of these minerals This explain these high values by a preferential assimilation of Ca and Al in the melt. The matrix away from *S4b* antigorite veins does not contain any serpentine. On the contrary, the Raman spectra of the pseudotachylyte matrix located close to *S4b* veins (< 0.6 mm) display characteristic peaks of antigorite at 229, 379, 461, 378 and 1045 cm^{-1} at low frequency and 3763 and 3700 cm^{-1} at high frequency (Fig. 6D). Additional peaks indicate the presence of olivine (331, 819 and 850 cm^{-1}) and clinopyroxene (1012 cm^{-1}).

Microlites of olivine are characterized by X_{Mg} values between 0.80 and 0.85, close to those of primary olivine (0.82). Clinopyroxene microlite composition is between augite and diopside.

Raman spectra of serpentine clasts from pseudotachylyte veins are characterized by peaks at 229, 377, 458, 683 and 1045 cm^{-1} at low frequency and at 3670 and 3700 cm^{-1} at high frequency (Fig. 6C), indicating a predominance of antigorite (Groppo et al., 2006; Reynard et al., 2015). Peaks at 819 and 850 cm^{-1} indicate the presence of olivine, likely in small amounts (Ishii, 1978; Piriou and MacMillan, 1983). Peaks at 1112 cm^{-1} indicate a small chrysotile component. Serpentine clasts and olivine clasts are characterized by similar X_{Mg} values around 0.82 (Table 2).

4.3. Dehydration of host rock serpentine along pseudotachylyte vein boundaries

4.3.1. Secondary olivine rims.

In thin sections cut in pseudotachylyte-bearing samples from localities 1 and 2, the host rock sides of pseudotachylyte veins are outlined by thin rims of olivine (Fig. 7A, B, C, E, F and G). Olivine rims are present where the host rock serpentine is in contact with the vein, but are absent where pseudotachylyte is in contact with pyroxene and spinel. The secondary olivine rims are observed along the boundaries of both fault veins and injection veins (Fig. 7A). Along fault veins, the thickness of secondary olivine rims, laterally variable, is between 70 and 500 µm for fault vein widths between 200 µm and 5 mm. Along injection veins, the thickness of the secondary olivine rims, also laterally variable, is between 70 and 300 µm, for vein widths of about 1 mm or less. The secondary olivine habitus consists of crystals displaying dendritic to acicular shapes or more rarely stubby euhedral shapes (Fig. 7B, C and G). Dendritic olivine is the most common habitus. The dendrites rarely exceed 15 µm in length. In euhedral to subhedral secondary olivine, variations in gray color intensity in the SEM images (Fig. 7G) reflect variations in the Mg number (between 61 and 74, Table. 1). Where the pseudotachylyte vein-host rock boundary is cataclastic, secondary olivine is rare, cataclastic, and the fragments are mixed within serpentine and pyroxene clasts, confirming that cataclasis can post-date pseudotachylyte formation and host-rock serpentine dehydration. Serpentinite survivor clasts in pseudotachylyte veins are surrounded by rims of secondary olivine (Fig. 7D). Secondary olivine is also observed along micro-fractures across clasts (Fig. 7D). Conversely, pyroxene and ilmenite clasts do not display any rim of olivine (Fig. 7B).

The X_{Mg} values of secondary olivine are between 0.61 and 0.74, that is, significantly lower than those of primary olivine which are 0.82 to 0.84 (Table 1). This indicates a significant substitution of Mg by Fe and, therefore, an origin of olivine different from those present in the host rock. The substitution is also observed in the secondary olivine from rims around serpentinite clasts with X_{Mg} values between 0.61 and 0.64, close to those measured in the olivine along pseudotachylyte boundaries (Fig. 7D). These significantly higher FeO contents in olivine around serpentinized clasts or along pseudotachylyte vein boundaries indicate an origin which is different from that of the host rock primary olivine.

Rims of secondary olivine are present where pseudotachylyte is not crossed by late stage serpentine veins (Fig. 2C). Where late serpentine veins (stage S4b) cross-cut pseudotachylyte veins, the pseudotachylyte is affected by serpentinization (Fig. 2C). The nearby host rock is also invaded on a width of about 1 cm.

4.3.2. Post-seismic serpentinization.

The pseudotachylyte veins and secondary olivine rims are cross-cut by late serpentine veins (Fig. 2). These veins have a thickness which does not exceed 250 µm and a lateral extension limited to a few centimeters. The boundaries are sharp. Characteristic Raman peaks at 229, 378, 460, 639, 681 and 1045 cm^{-1} at low frequency and by 3669 and 3701 cm^{-1} at high frequency indicate that the veins are composed of antigorite with a slight proportion of chrysotile, as attested by a minor peak at 1112 cm^{-1} (Fig. 6B; Rinaudo and Gastaldi, 2003; Auzende et al., 2004; Groppo et al., 2006). On both sides of the antigorite veins, a whitish serpentinization affects the host rock as well as the crossed pseudotachylyte veins over a thickness between 1 and 2.5 mm (Fig. 2). The thickness of the serpentinization halo is proportional to that of the cross-cutting antigorite vein.

In the serpentinization haloes, the unaltered minerals (i.e., preserved during the three first serpentinization stages) are entirely serpentinized (Fig. 3C) by an assemblage of antigorite and chrysotile, as attested in the Raman spectra by peaks at 229, 378, 461, 639, 681, 1047 and 1112 cm^{-1} at low frequency and at 3671 and 3700 cm^{-1} at high frequency (Fig. 6D). Where antigorite veins cross-cut pseudotachylyte veins, the pseudotachylyte matrix and olivine and pyroxene microlites are replaced by a similar assemblage of antigorite ± chrysotile, as indicated by the presence of characteristic peaks in the Raman spectra at 229, 379, 461, 638, 681, 1045 and 1112 cm^{-1} at low frequency and at 3763 and 3700 cm^{-1} at high frequency (Fig.6E). Additional peaks, respectively at 667 and 1012 cm^{-1} at high frequency and at 821 and 843 cm^{-1} at low frequency indicate the presence of relict diopside and olivine in the serpentinization halo.

5. Discussion.

5.1. Relative chronology of serpentinization events and geodynamic significance.

The first three stages of serpentinization S1, S2 and S3 described by Debret (2013) are characterized by the presence of low-temperature and low-pressure serpentine polymorphs. This suggests that these stages occurred during sea floor spreading of the Piemonte-Liguria oceanic lithosphere and concurrent mantle hydration. Stage *S4* succeeding to the first three stages is characterized by the presence of antigorite, which is a high-pressure serpentine polymorph (Ulmer and Trommsdorff, 1995; Wunder and Schreyer, 1997; Evans, 2004; Guillot et al., 2015). It is proposed here that stage *S4* occurred at depth during the subduction of the Piemonte-Liguria lithosphere (Fig. 8).

The presence in not serpentinized pseudotachylyte veins of partly or entirely serpentinized antigorite-bearing clasts surrounded by rims of secondary olivine clearly indicates that the seismic ruptures at the origin of the pseudotachylyte veins took place while stage *S4* antigorite was stable. At the peak pressure and temperature conditions recorded by the Monte Maggiore metagabbro dykes (450°C and 0.85 GPa; Nicollet et al., 2001), antigorite is stable. However, antigorite may have started to form before the serpentinized peridotite reached the peak conditions recorded by the metagabbro assemblages. Indeed, according to Guillot et al. (2015), the minimum pressure at which antigorite becomes stable is 0.7 GPa, for a temperature of *ca*. 315°C. It follows that *S4* (more precisely *S4a*) serpentinization could have taken place at pressures between 0.7 and 0.85 GPa, that is at depths between *ca*. 20 km and *ca*. 30 km (with a mean serpentinized peridotite density of 3000 kg.m^{-3}). Stage *S4b* serpentine veins cross-cutting pseudotachylyte veins (Fig. 8) consist of antigorite, meaning that the Monte Maggiore pseudotachylyte at localities 1 and 2 formed under pressure conditions at which antigorite was still stable. These observations are in agreement for a formation of the Monte Maggiore pseudotachylyte in a subducting slab at depths of 20~30 km.

In pseudotachylyte veins from the Cima di Gratera unit, Austrheim and Andersen (2004) and Andersen and Austrheim (2006) report serpentinite clasts whose rims are partly surrounded by newly crystallized olivine. Although the Mg content of these rims (X_{Mg} ~ 0.90; Austrheim and Andersen, 2004) significantly differs from what is observed at Monte Maggiore (X_{Mg} values between 0.61 and 0.64), it seems that secondary dehydration of hydrated ultramafic clasts is also preserved in the Cima di Gratera unit. A similar conclusion can be reached regarding the pseudotachylyte veins formed under eclogite facies conditions in the Moncuni metaperidotite, Lanzo massif. Indeed, although the depth at which the paleo-earthquakes took place is larger in the Moncuni case than in the Monte Maggiore case (60~70 km *vs*. 20~30 km), Scambelluri et al. (2017) report the presence of antigorite in pseudotachylyte-hosted ultramafic clasts, showing that secondary dehydration of hydrated ultramafic clasts is preserved at Moncuni. Besides, Scambelluri et al. (2017) report the presence, in metaperidotite, of metamorphic olivine formed by the reaction, under eclogite facies conditions.

antigorite + brucite → olivine + fluid.

Since it is not observed only along pseudotachylyte veins, this secondary olivine is clearly metamorphic in origin and is not related to co-seismic slip, at variance with the interpretation presented here.

5.2. ‘’Co-seismic’’ origin of secondary olivine.

Secondary olivine is characterized by X_{Mg} values between 0.61 and 0.74 These values are higher than the X_{Mg} values between 0.82 and 0.84 obtained on primary olivine in the host serpentinized peridotite. This difference in X_{Mg} values can be explained by a preferred assimilation of iron by magnetite commonly associated to antigorite ± chrysotile assemblages in the host rock and indicates that the secondary olivine and the primary magmatic olivine have different origins. Moreover, the presence of rims of iron-rich secondary olivine around most of the serpentine survivor clasts (Fig. 7D) demonstrates that the same process of dehydration as that observed along the vein boundaries was active around clasts. These observations show a synchronicity between formation of secondary olivine and formation of the pseudotachylyte. It follows that the secondary olivine results from dehydration of serpentine, the heat necessary for dehydration being provided by the co-seismic frictional melt.

5.3. Are secondary olivine rims the result of dehydration embrittlement?

Dehydration embrittlement requires temperature conditions between 500 and 720°C (610 ± 110°C) to dehydrate antigorite into forsterite + talc + H_20 (Ulmer and Trommsdorff, 1995; Peacock, 2001). In the Monte Maggiore unit, the peak temperature and pressure conditions recorded in gabbro dykes are 450°C and 0.85 GPa (Fig. 9; Nicollet et al., 2001). These conditions do not allow dehydration of serpentine (Ulmer and Trommsdorff, 1995; Wunder and Schreyer, 1997). Moreover, no mineral assemblages characterizing regional metamorphic dehydration (enstatite + olivine + Ti-clinohumite + talc; Hoogerduijn-Strating and Vissers, 1991; Scambelluri et al., 1991; Healy et al., 2009) were observed in the Monte Maggiore unit. Therefore, the formation of secondary olivine cannot be associated to a regional metamorphic dehydration such as the one invoked for dehydration embrittlement.

5.4. Other examples of transient thermo-mechanical effects induced by co-seismic frictional melting

The transient thermal effect induced by co-seismic frictional melt on the host hydrated peridotite described here is reminiscent of similar transient thermo-mechanical effects observed in other pseudotachylyte vein occurrences. Three examples are given below. (1) In the immediate vicinity of pseudotachylyte fault veins crossing quartz-feldspar rocks (quartzite and tonalite) in the Alps, Bestmann et al. (2012) describe 50 to 150 μm thick micro-shear zones consisting of ultrafine-grained quartz characterized by a crystal plastic deformation. This ductile deformation was made possible in an otherwise brittle environment by high differential stresses and temperature transients induced by frictional heating for a very short time span (a few seconds) during seismic rupture propagation. Regarding the tonalite case and using TitaniQ thermometry, Bestmann et al. (2016) show that the quartz filling the micro-shear zones was initially deposited by an overheated fluid during the initial stages of co-seismic slip before being plastically deformed. (2) Pittarello et al. (2008) report healed micro-fractures in plagioclase clasts contained in pseudotachylyte related to the Gole Larghe fault zone crossing the Adamello batholith in the Italian Alps. Micro-fracture formation and subsequent healing are inferred to be contemporaneous with co-seismic slip. (3) Heterogeneous melting distribution described by Griffith et al. (2010) along wavy faults in granodioritic and tonalitic host rocks are explained by transient stress perturbations during co-seismic slip propagation. Frictional melt is preferentially formed along contractional bends because of enhanced normal stresses and tends to accumulate in extensional bends.

5.5. Estimation of the amount of water released by co-seismic serpentine dehydration

At the scale of a subducting slab, especially those slabs formed by slow to ultra-slow oceanic accretion, the in-situ co-seismic dehydration process described here can play a major role in fluid transfers, depending on the size of the rupture surface. Besides, if co-seismic dehydration is considered at the scale of the Wadati-Benioff zone, a significant volume of water can be released by repeated earthquakes. The dehydration reaction serpentine → olivine + talc + H_2O leads to the release of 13 wt.% of water. The amount of water released during propagation of a seismic rupture and slip across a serpentinite mass can be estimated based on the volume of secondary olivine formed during this event. In the following, we attempt to estimate the amount of water released during frictional associated with seismic slip along a fault in serpentinite. The calculation is done in two steps. The first step, which is similar to the analysis followed by Wenk et al. (2000), consists of estimating the thickness of an 'ideal' single pseudotachylyte fault vein that would form along an 'ideal' unique rupture surface. The second step aims at determining the volume of water released by host rock dehydration, based on the thickness of the pseudotachylyte vein that forms in the serpentinized peridotite. Before giving the details of the calculation, the various assumptions and simplifications necessary for the computation are listed below.

5.5.1. Assumptions and simplifications

(1) As mentioned above, the computation is done for an 'ideal' unique fault vein that would form along an 'ideal' unique rupture surface. We therefore neglect the complexity of pseudotachylyte networks reported by many researchers (e.g., Swanson, 1988; Fabbri et al., 2000; Allen, 2005; Di Toro and Pennacchioni, 2005; Rowe et al., 2018).

(2) For the same sake of simplicity as (1), injection veins and associated dehydration are neglected.

(3) The rupture is supposed to nucleate in and propagate across serpentinized peridotite.

(4) The ambient temperature of the serpentinized peridotite hosting the rupture is assumed at 450°C (Nicollet et al., 2001).

(5) The computation is done for a magnitude 6 earthquake. The rupture surface area for such an *M*6 event is typically 100 km^2 (Hanks and Bakun, 2014).

(6) The energy released during the earthquake is mostly converted to heat.

(7) The seismic efficiency η (irradiated energy/total released energy ratio, E_s/E_{tot}) is assumed to be 0.24% (McGarr et al., 1979).

(8) The proportion of survivor clasts is about 10%.

(9) The frictional melt is not super-heated (Di Toro and Pennacchioni, 2004).

(10) The density of the serpentinized peridotite is 3000 kg.m^{-3}.

5.5.2. Calculation of the thickness of an 'ideal' single pseudotachylyte vein

Following the calculation of Wenk et al. (2000), we compute the total energy released by the earthquake assuming that most of the energy is converted to heat (assumption (6)). Besides, we compute the energy required to melt one mass unit of peridotite. The total energy released E_{tot} is obtained from E_s, itself obtained from the relationship between surface magnitude M_s and irradiated energy E_s ($\log E_s = 4{,}4 + 1{,}5\ M_s$, E_s in J; Choy and Boatwright, 1995), recalling that the moment magnitude and the surface magnitude are almost identical given the accuracy required here (Das et al., 2011).

We obtain $E_s = 10^{13.4}$ J.

Assuming a seismic efficiency η of 0.24% (assumption (7)), $E_{tot} = E_s/\eta = 1.046 \times 10^{16}$ J.

The energy to melt one mass unit of serpentinized peridotite is:

$E_{mu} = C_p\,(T_{melt} - T_{initial}) + \Delta H$

Where C_p is the specific heat at constant pressure (1000 J.K^{-1}.kg^{-1}; Kojitani and Akaogi, 1997), T_{melt} is the melting temperature (1700°C; Kojitani and Akaogi, 1997), $T_{initial}$ is the ambient temperature (450°C), and ΔH is the heat of fusion (6×10^5 J.kg^{-1}; Kojitani and Akaogi, 1997). Numerical application gives $E_{mu} = 1.85 \times 10^6$ J.

If the proportion of unmelted clasts is about 10% (assumption (8)), the energy required for melting 1 kg of rock becomes $E_{mucorr} = 1.665 \times 10^6$ J.

Dividing E_{tot} by E_{mucorr} gives the mass of pseudotachylyte generated during the *M*6 event, that is,

6.28×10^9 kg, corresponding to a volume of 2.09×10^6 m^3 with a serpentinized peridotite density of 3000 $kg.m^{-3}$ (assumption (10)).

Assuming that this volume is uniformly distributed over the 100 km^2 of the rupture area through the serpentinized peridotite, the thickness of the 'ideal' fault vein should be 2.09×10^{-2} m = 2.09 cm.

5.5.3. Calculation of the quantity of released water.

The water content of serpentine, whatever the polymorph, is about 13 wt %. Optical microscope and SEM observations suggest that the ratio between the fault vein thickness and the width of the dehydrated serpentinite rim on the two sides of the vein is between 0.2 and 0.8, the mean value being 0.5.

Isolating 1 m^2 of fault vein inside the serpentinized peridotite, the 2.09 cm thick pseudotachylyte vein would dehydrate a layer of serpentine of 1.045 cm thickness. For one square meter of rupture in the serpentinized peridotite, the maximum amount of released water would be: 1.045×10^{-2} m x 13×10^{-2} x 1 m^2 = 13.585×10^{-4} m^3 ~ 1.36 L. If dehydration takes place over the entire rupture surface, the total volume of released water would reach 1.36×10^5 m^3.

5.6. Fate of the water released by co-seismic dehydration of serpentine

Regarding the fate of the water released by co-seismic dehydration of serpentine, two end-member scenarios can be considered. (1) As soon as it is released, the water is entirely incorporated (dissolved) in the melt. (2) All the released water escapes from the slip surface. The actual scenario is likely intermediate between these two end-member cases.

Observations or arguments in favor of scenario (1) are as follows:

- Thermodynamical calculations (Katz et al., 2003) indicate that the weight fraction of H_2O dissolved in a peridotite-derived melt increases with pressure. While it is zero at atmospheric pressure, it reaches ~13 wt.% at 1 GPa (Dixon et al., 1995; Mysen and Wheeler, 2000).
- According to Andersen and Austrheim (2006), the Cima di Gratera pseudotachylytes are characterized by a high fluid (water) content, as testified by micro-vesicularity in the vein matrix.

These considerations indicate that a total or nearly total assimilation of the released water by the co-seismic melt is possible.

If the end-member scenario (2) is valid, then the released water can have various effects, depending on the path it will follow. (i) If the water percolates upwards, it should reach the upper plate and should contribute, with other released fluids, to hydration of the mantle wedge, eventually leading to magma genesis and arc volcanism. (ii) If the water percolates upwards along the subduction interface between the subducting and overlying plates, it can influence the rheology of the rocks present there, enhance chemical transfers and contribute to metasomatic or metamorphic reactions (Angiboust and Agard, 2010; Scambelluri et al., 2015; Bebout and Penniston-Dorland, 2016; Agard et al., 2018). (iii) Local accumulations of fluid along the interface can also trigger slow earthquakes as often observed at depths larger than the down-dip limit of the seismogenic (locked) portions of many subduction zones (Hirose et al., 2010; Obara, 2010; Beroza and Ide, 2011; Franck et al., 2015). (iv) Last but not least, if the released water remains along or near the co-seismic slip surface but without being incorporated in the co-seismic melt, it could, due to its possibly abnormally high pressure at the considered depths, trigger aftershocks. Indeed, since the early work of Nur and Brooker (1972), several observations suggest that over-pressured fluids migrating along or near seismic fault surfaces may be responsible for aftershocks (Li et al., 1987; Bosl and Nur, 2002; Cox and Ruming, 2004; Miller et al., 2004; Micklethwaite, 2008; Waldhauser et al., 2012). The observations described here provide a possible mechanism that could account for fluid-related aftershocks in hydrated mantle rocks. The water released after a large-magnitude event could locally increase the pore pressure and subsequently trigger aftershocks in the vicinity of the main seismogenic fault. The tiny pseudotachylyte veins secant on larger veins observed at localities 1 and 2 could be the result of the largest seismic ruptures among the otherwise small magnitude aftershocks.

6. Conclusion

The Monte Maggiore serpentinized peridotites host pseudotachylyte fault veins, showing that seismic ruptures can propagate through hydrated mantle rocks (serpentinized peridotite or serpentinite). A similar observation has already been reported by Tarling et al. (2018). Such a propagation through a partly hydrated mantle rock can also be inferred from the works of Andersen and Austrheim (2006) and Scambelluri et al. (2017) who describe serpentine-bearing survivor clasts in pseudotachylyte veins from the Cima di Gratera or the Moncuni ultramafic units. However, these observations are not precise enough to demonstrate whether the seismic ruptures nucleated in hydrated mantle rocks or whether they nucleated in non-hydrated rocks (peridotite or gabbro for instance) before propagating through serpentinized peridotite or serpentinite.

Microstructural, petrological and geochemical studies of the Monte Maggiore ultramafic pseudotachylyte veins and their host rock lead to the following results:

1) Along the contact surfaces with pseudotachylyte veins, the host serpentinized peridotite is outlined by rims of secondary olivine resulting from serpentine dehydration induced by frictional heating during seismic faulting.
2) Pseudotachylyte veins include antigorite-bearing clasts and are cross-cut by antigorite veins, indicating that they were formed at pressure and temperature conditions under which antigorite is stable. These conditions consist of a minimum pressure of 0.7 GPa, that is, a minimum depth of ~ 20 km. The maximum depth of formation of antigorite and of pseudotachylyte is constrained by the peak pressure condition recorded by gabbro (0.85 GPa) and is ~30 km.
3) The iron content in secondary olivine is higher than in the primary mantle olivine. The iron enrichment can be accounted for by the reaction magnetite + serpentine (+ brucite + H_2) → olivine + H_20 during the frictional melting-induced dehydration process, magnetite itself being a product of the hydration reaction of pristine mantle olivine.

Assuming an earthquake of magnitude 6 and a simplified model for the Monte Maggiore fossil earthquakes , we estimate, the volume of water released by co-seismic dehydration is estimated at ~ 1.4 L for one square meter of rupture in a serpentinized peridotite for a magnitude 6 event. For the same event, if dehydration takes place over the entire rupture surface (100 km^2), the total volume of released water is estimated at ~ 1.36×10^5 m^3. The fate of this water is unknown. It can be entirely assimilated by the melt. Alternatively, it can escape from the seismogenic fault and contribute to mantle wedge hydration or to fluid-rock interactions along the plate interface. It can also play a role in the delayed triggering of slow earthquakes along the plate interface or in the triggering of aftershocks immediately after a large seismic event.

Acknowledgments.

This work was funded by the CNRS-INSU TelluS-ALEAS program. Scanning electron microscopy was supported by the RENATECH network and CRPG (UMR 7358). Constructive comments from two anonymous reviewers helped clarifying the initial version of the manuscript.

References.

Agard, P., Plunder, A., Angiboust, S., Bonnet, G., Ruh, J., 2018. The subduction plate interface: Rock record and mechanical coupling (from long to short time scales). Lithos 320 – 321, 537 – 566. https://doi.org/ 10.1016/j.lithos.2018.09.029.

Allen, J.L., 2005. A multi-kilometer pseudotachylyte system as an exhumed record of earthquake rupture geometry at hypocentral depths (Colorado, USA). Tectonophysics 402, 37 – 54. https://doi.org/10.1016/j.tecto.2004.10.017.

Andersen, T.B., Austrheim, H., 2006. Fossil earthquakes recorded by pseudotachylytes in mantle peridotites from the Alpine subduction complex of Corsica. Earth and Planetary Science Letters 242, 58 – 72.

Andersen, T.B., Mair, K., Austrheim, H., Podladchikov, Y.Y., Vrijmoed, J.C., 2008. Stress release in exhumed intermediate and deep earthquakes determined from ultramafic pseudotachylyte. Geology 36, 995 – 998.

Andersen, T.B., Austrheim, H., Deseta, N., Silkoset, P., Ashwal, L.D., 2014. Large subduction earthquakes along the fossil Moho in Alpine Corsica. Geology 42, 395 – 398. https://doi.org/10.1130/G35345.1

Andréani, M., Mével, C., Boullier, A.M., Escartín, J., 2007. Dynamic control on serpentinite crystallization in veins: Constraints on hydration processes in oceanic peridotites. Geochemistry Geophysics Geosystems 8. https://doi.org/10.1029/2006GC001373.

Angiboust, S., Agard, P., 2010. Initial water budget: The key to detaching large volumes of eclogitized oceanic crust along the subduction channel? Lithos 120, 453 – 474. https://doi.org/10.1016/j.lithos.2010.09.007.

Austrheim, H., Andersen, T.B., 2004. Pseudotachylytes from Corsica: fossil earthquakes from a subduction complex. Terra Nova 16, 193 – 197. https://doi.org/10/1111/j.1365-3121.2004.00551.x.

Auzende, A.L., Daniel, I., Reynard, B., Lemaire, C., Guyot, F., 2004. High-pressure behavior of serpentine minerals: a Raman spectroscopic study. Physics and Chemistry of Minerals 31, 269 – 277.

Bebout, G.E., Penniston-Dorland, S.C., 2016. Fluid and mass transfer at subduction interfaces – The field metamorphic record. Lithos 240 – 243, 228 – 258. https://doi.org/10.1016/j.lithos.2015.10.007.

Beroza, G.C., Ide, S., 2011. Slow earthquakes and nonvolcanic tremor. Annual Review of Earth and Planetary Sciences 39, 271 – 296. https://doi.org/10.1146/annurev-earth-040809-15253.

Bestmann, M., Pennacchioni, G., Nielsen, S., Göken, M., De Wall, H., 2012. Deformation and ultrafine dynamic recrystallization of quartz in pseudotachylyte-bearing brittle faults: A matter of a few seconds. Journal of Structural Geology 38, 21 – 38. https://doi.org/10.1016/j.jsg.2011.10.001.

Bestmann, M., Pennacchioni, G., Mostefaoui, S., Göken, M., de Wall, H., 2016. Instantaneous healing of micro-fractures during coseismic slip: Evidence from microstructure and Ti in quartz geochemistry within an exhumed pseudotachylyte-bearing fault in tonalite. Lithos 254, 84 – 93. https://doi.org/10.1016/j.lithos.03.011.

Bosl, W.J., Nur, A., 2002. Aftershocks and pore fluid diffusion following the 1992 Landers earthquake. Journal of Geophysical Research 107, 2366. https://doi.org/10.1029/2001JB000155.

Choy, G.L., Boatwright, J.L., 1995. Global patterns of radiated seismic energy and apparent stress. Journal of Geophysical Research 100, 18205 – 18228.

Cox, S.F., Ruming, K., 2004. The St Ives mesothermal gold system, Western Australia-a case of golden aftershocks? Journal of Structural Geology 26, 1109 – 1125.

Das, R., Wason, H.R., Sharma, M. L., 2011. Global regression relations for conversion of surface wave and body wave magnitudes to moment magnitude. Natural Hazards 59, 801 – 810.

Debret, B., 2013. Serpentinites, vecteurs des circulations fluides et des transferts chimiques de l'océanisation à la subduction : exemple dans les Alpes occidentales. Clermont-Ferrand University PhD Thesis, 454 pp.

Debret, B., Nicollet, C., Andreani, M., Schwartz, S., Godard, M., 2013. Three steps of serpentinization in an eclogitized oceanic serpentinization front (Lanzo Massif – Western Alps). Journal of Metamorphic Geology 31, 165 – 186. https://doi.org/10.1111/jmg.12008.

Deseta, N., Andersen, T.B., Ashwal, L.D., 2014. A weakening mechanism for intermediate-depth seismicity? Detailed petrographic and microstructural observation from blueschist facies pseudotachylytes, Cape Corse, Corsica. Tectonophysics 610, 138 – 149.

Di Toro, G., Pennacchioni, G., 2004. Superheated friction-induced melts in zoned pseudotachylytes within the Adamello tonalites (Italian Southern Alps). Journal of Structural Geology 26, 1783 – 1801.

Di Toro, G., Pennacchioni, G., 2005. Fault plane processes and mesoscopic structure of a strong-type seismogenic fault in tonalites (Adamello batholith, Southern Alps). Tectonophysics 402, 55 – 80.

Dixon, J., Stolper, E., Holloway, J., 1995. An experimental study of water and carbon dioxide solubilities in mid ocean ridge basaltic liquids: I. Calibration and solubility models. J. Petrol. 36, 1607 – 1631.

Dobson, D.P., Meredith, P.G., Boon, S.A., 2002. Simulation of subduction zone seismicity by dehydration embrittlement. Science 298, 1407 – 1410.

Evans, B.W., 2004. The serpentinite multisystem revisited: chrysotile is metastable. International Geology Review 46, 479 – 506.

Fabbri, O., Lin, A., Tokushigé, H., 2000. Coeval formation of cataclasite and pseudotachylyte in a Miocene forearc granodiorite, southern Kyushu, Japan. Journal of Structural Geology, 22 1015 – 1025.

Fabbri, O., Magott, R., Fournier, M., Etienne, L., 2018. Pseudotachylyte in the Monte Maggiore ophiolitic unit (Alpine Corsica): A lateral extension of the Cima di Gratera intermediate-depth Wadati-Benioff paleo-seismic zone. Bulletin de la Société Géologique de France 189, 1 – 17. https://doi.org/10.1051/bsgf/2018020.

Ferrand, T., Hilairet, N., Incel, S., Deldicque, D., Labrousse, L., Gasc, J., Renner, R., Wang, Y., Green, H.W., 2017. Dehydration-driven stress transfer triggers intermediate-depth earthquakes. Nature Communications 8, 15247 – 15258.

Frank, W.B., Shapiro, N.M., Husker, A.L., Kostoglodov, V., Bhat, H.S., Campillo, M., 2015. Along-fault pore-pressure evolution during a slow-slip event in Guerrero, Mexico. Earth and Planetary Science Letters 413, 135 – 143. https://doi.org/10.1016/j.epsl.2014.12.051.

Griffith, W.A., Nielsen, S., Di Toro, G., Smith, S.A., 2010. Rough faults, distributed weakening, and off-fault deformation. Journal of Geophysical Research 115, B08409. https://doi.org/10.1029/2009JB006925.

Groppo, C., Rinaudo, C., Cairo, S., Gastaldi, D., Compagnoni, R., 2006. Micro-Raman spectroscopy for a quick and reliable identification of serpentine minerals from ultramafics. European Journal of Mineralogy 18, 319 – 329.

Guillot, S., Schwartz, S., Reynard, B., Agard, P., Prigent, C., 2015. Tectonic significance of serpentinites. Tectonophysics 646, 1 – 19.

Hacker, B. R., Peacock, S.M., Abers, G.A., Holloway, S.D., 2003. Subduction Factory 2. Are intermediate-depth earthquakes in subducting slabs linked to metamorphic dehydration reactions? Journal of Geophysical Research 108. https://doi.org/10.1029/2001JB001129.

Hanks, T.C., Bakun, W.H., 2014. M–log A models and other curiosities. Bulletin of the Seismological Society of America 104, 2604 – 2610.

Healy, D., Reddy, S.M., Timms, N.E., Gray, E.M., 2009. Trench-parallel fast axes of seismic anisotropy due to fluid-filled cracks in subducting slabs. Earth and Planetary Science Letters 283, 75 – 86.

Hirose, H., Asano, Y., Obara, K., Kimura, T., Matsuzawa, T., Tanaka, S., Maeda, T., 2010. Slow earthquakes linked along dip in the Nankai subduction zone. Science 330, 1502 – 1502.

Hoogerduijn-Strating, E.H., Vissers, R.L.M., 1991. Dehydration-induced fracturing of eclogite-facies peridotites: implication for the mechanical behavior of subduction oceanic lithosphere. Tectonophysics 200, 187 – 198.

Houston, H., 2015. Deep Earthquakes. In: G. Schubert (editor) Treatise on Geophysics, 2nd edition, Vol. 4. Elsevier, Oxford, 329-354.

Ishii, K., 1978. Lattice dynamics of forsterite. American Mineralogist 63, 1198 – 1208.

Jackson, M.D., Ohnenstetter, M., 1981. Peridotite and gabbroic structures in the Monte Maggiore massif, Alpine Corsica. The Journal of Geology 89, 703 – 719.

Jung, H., Green, H.W., Dobrzhinetskaya, L.F., 2004. Intermediate-depth earthquake faulting by dehydration embrittlement with negative volume change. Nature 428, 545 – 549.

Katz, R.F., Spiegelman, M. Langmuir, C.H., 2003. A new parameterization of hydrous mantle melting. Geochemistry, Geophysics, Geosystems, 4, 1073. https://doi.org/10.1029/2002GC000433.

Kita, S., Ferrand, F., 2018. Physical mechanisms of mantle earthquakes: Comparison of natural and experimental events. Scientific Reports 8, 17049. https://doi.org/10.1038/s41598-018-35290-x.

Kojitani, H., Akaogi, M., 1997. Melting enthalpies of mantle peridotite: calorimetric determinations in the system CaO-MgO-Al_2O_3-SiO_2 and application to magma generation. Earth and Planetary Science Letters 153, 209 – 222.

Lagabrielle, Y., Lemoine, M., 1997. Alpine, Corsican and Apennine ophiolites: the slow-spreading ridge model. Comptes Rendus de l'Académie des Sciences 325, 909 – 920.

Lahondère J.C., 1992. Carte géologique de la France au 1/50000. Feuille de Luri. BRGM.

Li, V.C., Seale, S.H., Cao, T., 1987. Post-seismic stress and pore pressure readjustment and aftershock distributions. Tectonophysics 144, 37-54.

Magott, R., 2016. Propagation de la rupture sismique dans la lithosphère océanique: une étude basée sur l'analyse structurale des cataclasites et pseudotachylytes jalonnant les failles dans les roches mafiques et ultramafiques accrétées ou obductées sur les continents. L'exemple corse. Franche-Comté University PhD Thesis, 255 pp.

Magott, R., Fabbri, O., Fournier, M., 2016. Subduction zone intermediate-depth seismicity: Insights from the structural analysis of Alpine high-pressure ophiolite-hosted pseudotachylytes (Corsica, France). Journal of Structural Geology 87, 95 – 114. https://doi.org/10.1016/j.jsg.2016.04.002.

Magott, R., Fabbri, O., Fournier, M., 2017. Polyphase ductile/brittle deformation along a major tectonic boundary in an ophiolitic nappe, Alpine Corsica: Insights on subduction zone intermediate-depth asperities. Journal of Structural Geology 94, 240 – 257. https://doi.org/10.1016/j.jsg.2016.12.002.

Meresse, F., Lagabrielle, Y., Malavieille, J., Ildefonse, B., 2012. A fossil Ocean-Continent Transition of the Mesozoic Tethys preserved in the Schistes Lustrés nappe of northern Corsica. Tectonophysics 579, 4 – 16.

Manatschal, G., Müntener, O., 2009. A type sequence across an ancient magma-poor ocean-continent transition: the example of the western Alpine Tethys ophiolites. Tectonophysics 473, 4 – 19.

McGarr, A., Spottiswoode, S.M., Gay, N.C., Ortlepp, W.D., 1979. Observations relevant to seismic driving stress, stress drop, and efficiency. Journal of Geophysical Research 84, 2251 – 2261.

Mével, C., 2003. Serpentinization of abyssal peridotites at mid-ocean ridges. Comptes Rendus Geosciences 335, 825 – 852.

Micklethwaite, S., 2008. Optimally oriented ''fault-valve'' thrusts: Evidence for aftershock-related fluid pressure pulses? Geochemistry, Geophysics, Geosystems, 9, Q04012. https://doi.org/10.1029/2007GC001916.

Miller, S.A., Collettini, C., Chiaraluce, L., Cocco, M., Barchi, M., Kaus, B.J., 2004. Aftershocks driven by a high-pressure CO_2 source at depth. Nature, 427, 724 – 727.

Molli, G., Malavieille, J., 2011. Orogenic processes and the Corsica / Apennine geodynamic evolution: Insight from Taiwan. International Journal of Earth Science 100, 1207 – 1224. https://doi.org/10.1007/s00531-010-0598-y.

Molli, G., 2008. Northern Apennine-Corsica orogenic system: an updated overview. Geological Society, London, Special Publications 298, 413 – 442.

Mysen, B., Wheeler, K., 2000. Solubility behavior of water in haploandesitic melts at high pressure and high temperature. Am. Mineral., 85, 1128 – 1142.

Nakajima, J., Tsuji, Y., Hasegawa, A., Kita, S., Okada, T., Matsuzawa, T., 2009. Tomographic imaging of hydrated crust and mantle in the subducting Pacific slab beneath Hokkaido, Japan: Evidence for dehydration embrittlement as a cause of intraslab earthquakes. Gondwana Research 6, 470 – 481.

Nicollet, C., Chazot, G., Cloquet, C., 2001. Evolution géodynamique d'une portion du manteau : Pétrologie et trajet P-T des lherzolithes et gabbro associés du Monte Maggiore, Cap Corse. Journée de la Société Géologique de France, Clermont-Ferrand.

Nur, A., Booker, J.R., 1972. Aftershocks caused by pore fluid flow? Science 175, 885 – 887.

Obara, K., 2010. Phenomenology of deep slow earthquake family in southwest Japan: Spatio-temporal characteristics and segmentation. Journal of Geophysical Research 115, B00A25. https://doi.org/10.1029/2008JB006048.

Ohnenstetter, M., Ohnenstetter, D., Vidal, P., Cornichet, J., Hermitte, D., Mace, J. 1981. Crystallization and age of zircon from Corsican ophiolitic albitites: consequences for oceanic expansion in Jurassic times. Earth and Planetary Science Letters 54, 397 – 408.

Papa, S., Pennacchioni, G., Angel, R.J., Faccenda, M., 2018. The fate of garnet during (deep-seated) coseismic frictional heating: The role of thermal shock. Geology 46, 471 – 474. https://doi.org/10.1130/G40077.1.

Peacock, S.M., 2001. Are the lower plane of double seismic zones caused by serpentine dehydration in subducting oceanic mantle? Geology 29, 299 – 302.

Piccardo, G.B., Ranalli, G., Guarnieri, L., 2010. Seismogenic shear zone in the lithospheric mantle: Ultramafic pseudotachylyte in the Lanzo Peridotite (Western Alps, NW Italy). Journal of Petrology 51, 81 – 100.

Piccardo, G.B., Guarnieri, L., 2010. The Monte Maggiore peridotite (Corsica, France): a case study of mantle evolution in the Ligurian Tethys. Geological Society London Special Publications 337, 7 – 45.

Piriou, B., MacMillan, P., 1983. The high-frequency vibrational spectra of vitreous and crystalline orthosilicates. American Mineralogist 68, 426 – 443.

Pittarello, L., Di Toro, G., Bizzarri, A., Pennacchioni, G., Hadizadeh, J., Cocco, M., 2008. Energy partitioning during seismic slip in pseudotachylyte-bearing faults (Gole Larghe Fault, Adamello, Italy). Earth and Planetary Science Letters 269, 131 – 139.

Raleigh, C.B., Paterson, M.S., 1965. Experimental deformation of serpentinite and its tectonic implications. Journal of Geophysical Research 70, 3965 – 3985.

Rampone, E., Hofmann, A.W., Raczek, I., 2009. Isotopic equilibrium between mantle peridotite and melt: Evidence from the Corsica ophiolite. Earth and Planetary Science Letters 288, 601 – 610.

Rampone, E., Hofmann, A.W., 2012. A global overview of isotopic heterogeneities in the oceanic mantle. Lithos 148, 247 – 261.

Reynard, B., Bezacier, L., Caracas, R., 2015. Serpentines, talc, chlorites and their high-pressure phase transitions: a Raman spectroscopic study. Physics and Chemistry of Minerals 42, 641 – 649.

Rinaudo, C., Gastaldi, D., 2003. Characterization of chrysotile, antigorite and lizardite by FT-Raman spectroscopy. The Canadian Mineralogist 41, 883 – 890.

Rowe, C.D., Ross, C., Swanson, M.T., Pollock, S., Backeberg, N., Barshi, N.A., Bate, C.E., Carruthers, S., Coulson, S., Dascher-Cousineau, K., Harrichhausen, N., Peña Castro, A.F., Nisbet, H., Rakoczy, P., Scibek, J., Smith, H., Tarling, M.S., Timofeev, A., Young, E., 2018. Geometric complexity of earthquake rupture surfaces preserved in pseudotachylyte networks. Journal of Geophysical Research 123, 7998 – 8015. https://doi.org/10.1029/2018JB016192.

Rumori, C., Mellini, M., Viti, C., 2004. Oriented, non-topotactic olivine → serpentine replacement in mesh-textured, serpentinized peridotites. European Journal of Mineralogy, 16, 731 – 741.

Rutter, E.H., Brodie, K.H., 1988. Experimental ''syntectonic'' dehydration of serpentinite under condition of controlled pore water pressure. Journal of Geophysical Research 93, 4907 – 4932.

Scambelluri, M., Hoogerduijn-Strating, E.H., Piccardo, G., Vissers, R.L.M., Rampone, E., 1991. Alpine olivine and clinohumite-bearing assemblages in the Erro-Tobbio peridotite (Voltri Massif, NW Italy). Journal of Metamorphic Geology 9, 79 – 105.

Scambelluri, M., Pettke, T., Cannao, E., 2015. Fluid-related inclusions in Alpine high-pressure peridotite reveal trace element recycling during subduction-zone dehydration of serpentinized mantle. Earth and Planetary Science Letters 429, 45 – 59. https://doi.org/10.1016/j.epsl.2015.07.060.

Scambelluri, M., Pennacchioni, G., Gilio, M., Bestmann, M., Plümber, O., Nestola, F., 2017. Fossil intermediate-depth earthquakes in subducting slabs linked to differential stress release. Nature geoscience 10, 960 – 966.

Schmidt, M.W., Poli, S., 1998. Experimentally based water budgets for dehydrating slabs and consequences for arc magma generation. Earth and Planetary Science Letters 163, 361 – 379. https://doi.org/10.1016/S0012-821X(98)00142-3.

Swanson, M.T., 1988. Pseudotachylyte-bearing strike-slip duplex structures in the Fort Foster Brittle Zone, S. Maine. Journal of Structural Geology 10, 813 – 828.

Tarling, M.S., Smith, S.A.F., Viti, C., Scott, J.M., 2018. Dynamic earthquake rupture preserved in a creeping serpentinite shear zone. Nature communications 9, 3552. https://doi.org/10.1038/s41467-018-05965-0.

Ulmer, V., Trommsdorff, P., 1995. Serpentine stability to mantle depth and subduction-related magmatism. Science 268, 858 – 861.

Vitale-Brovarone, A., Beyssac, O., Malavieille, J., Molli, G., Beltrando, M., Compagnoni, R., 2013. Stacking and metamorphism of continuous segments of subducted lithosphere in a high-pressure wedge: The example of Alpine Corsica (France). Earth-Science Reviews 116, 35 – 56.

Viti, C., Mellini, M., 1998. Mesh textures and bastites in the Elba retrograde serpentinites. European Journal of Mineralogy 10, 1341 – 1359.

Waldhauser, F., Schaff, D.P., Diehl, T., Engdahl, R.E., 2012. Splay faults imaged by fluid-driven aftershocks of the 2004 M_w 9.2 Sumatra-Andaman earthquake. Geology 40, 243 – 246. https://doi.org/10.1130/G32420.1.

Wang, J., Zhao, D., Yao, Z., 2017. Seismic anisotropy evidence for dehydration embrittlement triggering intermediate-depth earthquakes. Scientific Reports 7, 2613 – 2622.

Wenk, H.R., Johnson, L.R., Ratschbacher, L., 2000. Pseudotachylites in the Eastern Peninsular Ranges of California. Tectonophysics 321, 253 – 277.

Wunder, B., Schreyer, W. (1997). Antigorite: High-pressure stability in the system $MgO-SiO_2-H_2O$ (MSH). Lithos, 41, 213 – 227. https://doi.org/10.1016/S0024-4937(97)82013-0.

Yamasaki, T., Seno, T., 2003. Double seismic zone and dehydration embrittlement of the subducting slab. Journal of Geophysical Research 108. https://doi.org/10.1029/2002JB001918.

Table captions

Table 1. Chemical composition of secondary olivine in dehydrated rims and host rock (serpentinized and non-serpentinized). NS: non-serpentinized, SP: serpentinized.

Table 2. Average composition of pseudotachylyte components.

Figure captions

Fig. 1. A: Simplified geological map of the study area (modified after Debret, 2013). B: A-A' cross-section.

Fig. 2. Relationships between *S4* serpentine veins, serpentinite host rock and pseudotachylyte veins. A. Late *S4b* fibrous antigorite (*Late Ant vein*) crossing pseudotachylyte (*Pst*) vein and serpentinite wallrock (*Serp wallrock*), locality 2. B. Zoned *S4b* antigorite vein (*Late Ant vein*) crossing partly serpentinized pseudotachylyte (*Serp Pst*) and serpentinized wallrock (*Serp wallrock*), locality 1. C. Late *S4b* antigorite vein (*Late Ant vein*) cross-cutting serpentinized peridotite and a pseudotachylyte vein. On each side of the antigorite vein, a serpentinization halo invades the wallrock. Invasion is deeper in the host serpentinite (about 750 μm) than in the pseudotachylyte (200 μm).

Fig. 3. Photographs of serpentinized peridotite outcrops and hand samples crossed by pseudotachylyte veins. A. Anastomosed fault vein network (*Pst networks*), locality 1. The veins show a positive relief. B. Isolated fault veins, locality 1. C. Serpentinite hand sample showing a fault vein (*Fv*) flanked by injection veins (*Iv*), locality 2. D. Serpentinitized peridotite (*Serp peridotite*) hand sample showing pseudotachylyte fault veins (*Pst*) and a pseudotachylyte vein-looking cataclastic zone (*Ct*), locality 2.

Fig. 4: Photomicrographs of pseudotachylyte and host serpentinite, locality 2. A. Flow folds in an injection vein reworking pyroxene and serpentinized olivine clasts (*Serp Ol clast*). B. Clast of reworked pseudotachylyte (*Pst clast*) with embayment (*Emb*). C. Pseudotachylyte matrix showing a polygonal texture due to devitrification. D. Pseudotachylyte fault vein (*Fv*) and associated injection vein (*Iv*). The serpentinite host rock below the fault vein is cataclastic (*Ct*). E. Pseudotachylyte fault vein (*Fv*) crossing a cataclastic serpentinite (*Ct*). F. Cataclastic serpentinite cross-cut by an early pseudotachylyte vein (*Early pst*) itself cross-cut by a late pseudotachylyte vein (*Late pst*).

Fig. 5. SEM images of pseudotachylyte veins in partly serpentinized peridotite, locality 1. A. Pseudotachylyte fault vein (*Pst*) with serpentinized wall rock. From the lower left corner of the image to its upper right corner, the size of microlites increases from the chilled margin (*Cm*, lower left) where microlites are small to the median part of the vein where microlites are larger (upper right). The square is the area enlarged in C. B. Rounded clasts of olivine displaying embayments. C. Clast of olivine (*Ol clast*) surrounded by olivine overgrowths with a comb structure. D. Clast of pseudotachylyte (*Pst clast*) reworked in a younger pseudotachylyte (*Pst*). Note the large embayment almost crossing the entire clast. E. Olivine and clinopyroxene microlites with acicular shapes near the chilled margin (*Cm*) or with lath shapes (near the median part of the vein). F. Enlargement of pseudotachylyte matrix showing rounded olivine clasts, acicular clinopyroxene microlites and serpentinized matrix (*Sz Matrix*).

Fig. 6. Raman spectra of serpentine phases obtained on pseudotachylyte fault veins, host rocks and late secant serpentine veins, locality 2. For each spectrum, the signal is analyzed on two acquisition spectral windows and the characteristic bands are indicated. A. Raman spectrum of the serpentinite hosting a pseudotachylyte vein and showing diffuse antigorite tentatively related to stage S4a (sample depicted in Fig. 3C). B. Raman spectrum of late antigorite veins related to stage S4b (sample depicted in Fig. 3C). The spectrum indicates a dominant antigorite composition and a minor chrysotile component. C. Raman spectrum of the central part of a serpentinite survivor clast reworked in a pseudotachylyte vein and surrounded by secondary olivine. The spectrum indicates the presence of stage S4a antigorite (diffuse in the clast and not under the form of vein filling). D. Raman spectrum indicating the presence of *S4b* antigorite in the serpentinized halo of the wall-rock at a distance of ~ 250 µm away from a late antigorite vein. E. Raman spectrum indicating the presence of *S4b* antigorite in the matrix of a pseudotachylyte vein crossed by a late antigorite vein. Raman analysis is done at a distance of ~ 250 µm from the antigorite vein.

Fig. 7. SEM images of secondary olivine rims along the boundaries between pseudotachylyte and host serpentinite or reworked clasts. A. Secondary olivine rim developed along the boundaries between host serpentinite (*Wall*) and injection and fault veins (*Pst*). To the left, the pseudotachylyte is in contact with ultracataclasite (*Uct*) itself in contact with cataclasite (*Ct*). Both cataclasite and ultracataclasite consist of fragments of serpentine mixed with fragments of secondary olivine. B. Secondary olivine rim (*Sec Ol*, right side of the image) showing clusters of dendritic secondary olivine (*DSO*) and acicular secondary olivine (*ASO*). Where it is not acicular or dendritic, the olivine is more massive, but the precise shape of the

crystals (euhedral or anhedral) cannot be determined. In the upper part of the image, a horizontal antigorite vein crossing (1) the serpentinite host rock (*Wall*), (2) the secondary olivine rim (*Sec Ol*) and (3) the pseudotachylyte vein (*Pst*) is attributed to the serpentinization stage S4b. *Il clast*: clast of ilmenite. C: Enlargement of the secondary olivine rim of (B) highlighting ~~the~~ dendritic secondary olivine (*DSO*) acicular secondary olivine (*ASO*). D. Antigorite rounded clast (*Ant Clast*) surrounded by a rim of secondary olivine (*Sec Ol*) in a pseudotachylyte vein (*Pst*). E. Secondary olivine rim (*Sec Ol*) along the boundary between serpentinite host rock (*Wall*) and a pseudotachylyte fault vein (*Pst*). The rectangle is the area enlarged in F. F. Secondary olivine rim (*Sec Ol*) displaying rectangular olivine crystals with long axes parallel to the host rock-pseudotachylyte vein (*Pst*) boundary. G. Secondary olivine rim (*Sec Ol*) between wall rock (*Wall*) and a pseudotachylyte vein (*Pst*). Inside the rim, differences in grey intensity reflects differences in the X_{Mg} of olivine crystals (between 0.61 and 0.69). Subhedral secondary olivines are best developed in the largest part of the dehydrated border.

Fig. 8. Relative chronology of serpentinization events and seismogenic ruptures. A. Fresh (i.e., not serpentinized) spinel peridotite equilibrated in the plagioclase domain before seafloor spreading (Piccardo and Guarnieri, 2010). B. First stages of serpentinization (stages S1 to S3) related to sea water-mantle rock interactions and characterized by low-pressure lizardite and chrysotile assemblages. C. High pressure serpentinization stage (stage S4a) characterized by the development of antigorite ± chrysotile assemblages at the expense of stages S1 to S3 lizardite and chrysotile assemblages. D. Seismic ruptures causing the formation of frictional melt and associated dehydration. E. Formation of antigorite veins (S4b) post-dating S1 to S4a serpentinization events and pseudotachylyte vein formation.

Fig. 9. P-T pathway of the Monte Maggiore peridotite unit projected on various mineralogical reactions (modified after Nicollet et al., 2001). Mantle upwelling refers to the adiabatic upwelling and decompression of the asthenosphere.

Fig. 10. Simplified geodynamical setting of co-seismic dehydration of serpentinite in the subducting Piemonte-Liguria oceanic lithosphere (Monte Maggiore unit) and associated water release. A. General sketch showing the eastward-dipping subduction of the Piemonte-Liguria oceanic plate under a micro-block or an island arc (Cretaceous to Paleogene times). B. Three scenarios of seismic rupture nucleation and propagation: (1) in non-hydrated peridotite, (2) in mixed non-hydrated and hydrated peridotite, (3) in hydrated peridotite. C. Co-seismic dehydration of hydrated peridotite at Monte Maggiore following scenario (3) and subsequent water release.

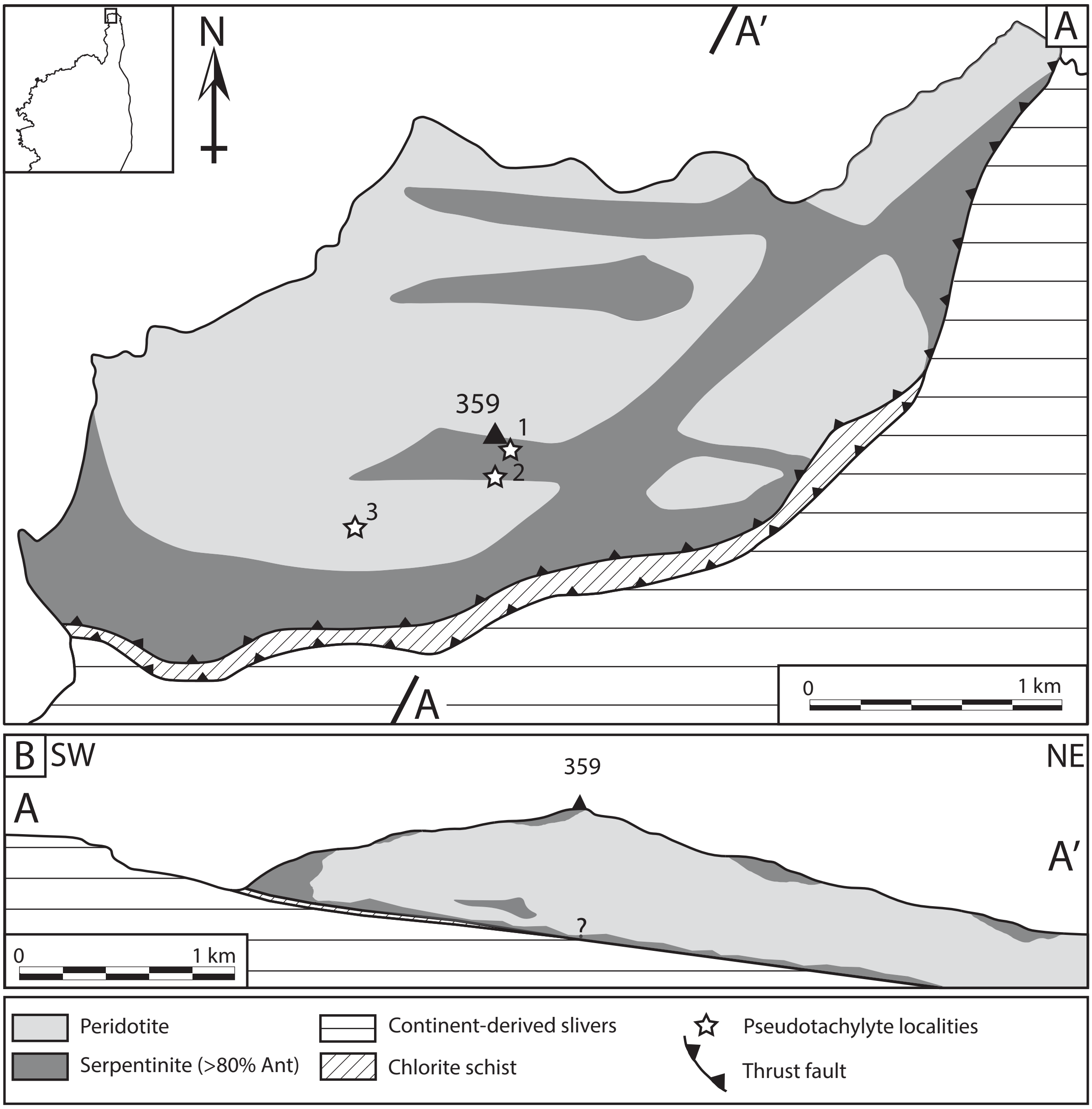
A
N
A′
359
1
2
3
A
0
1 km
B
SW
NE
359
A
A′
?
0
1 km
Peridotite
Serpentinite (>80% Ant)
Continent-derived slivers
Chlorite schist
Pseudotachylyte localities
Thrust fault

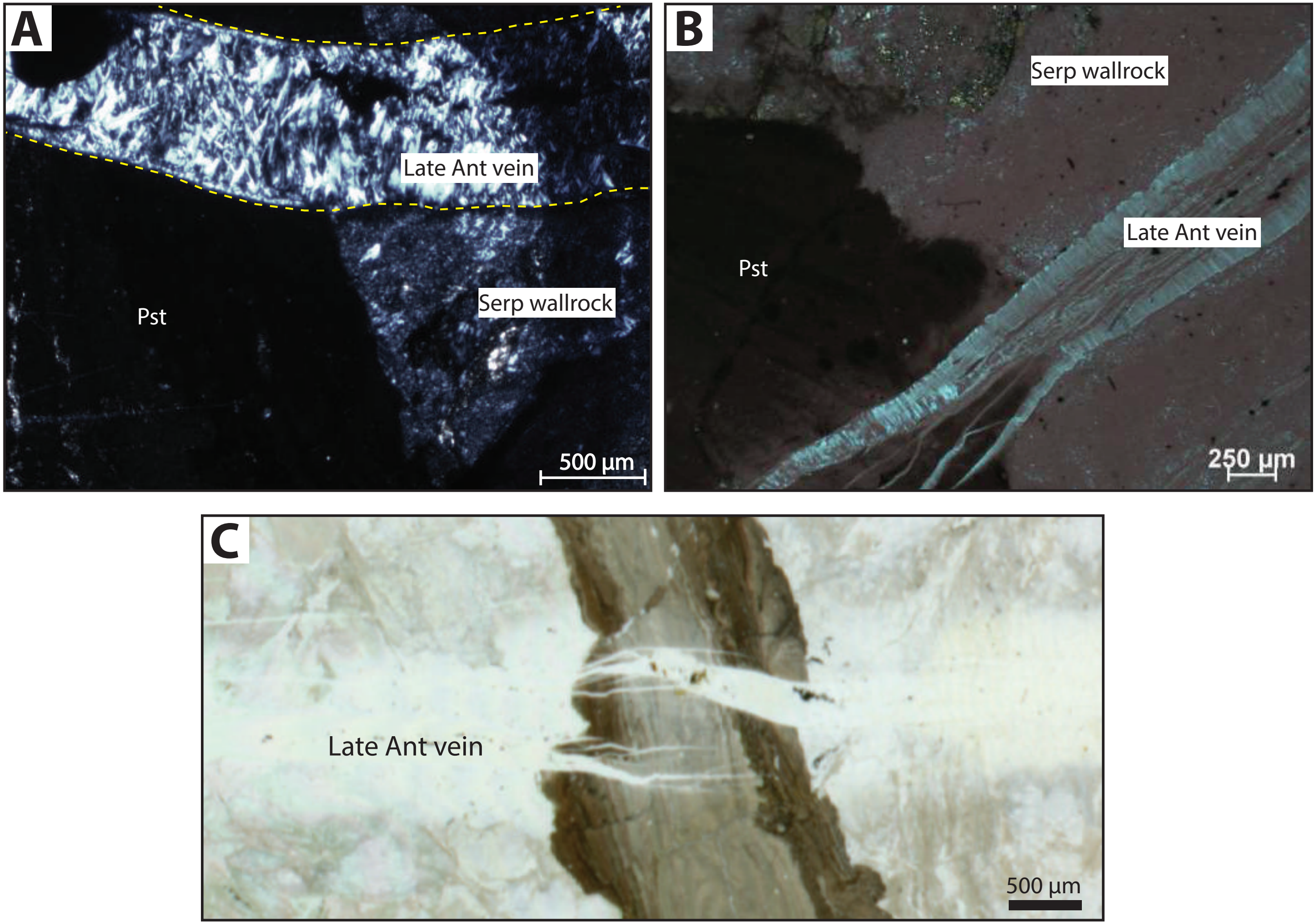
A
Late Ant vein
Pst
Serp wallrock
500 µm
B
Serp wallrock
Pst
Late Ant vein
250 µm
C
Late Ant vein
500 µm

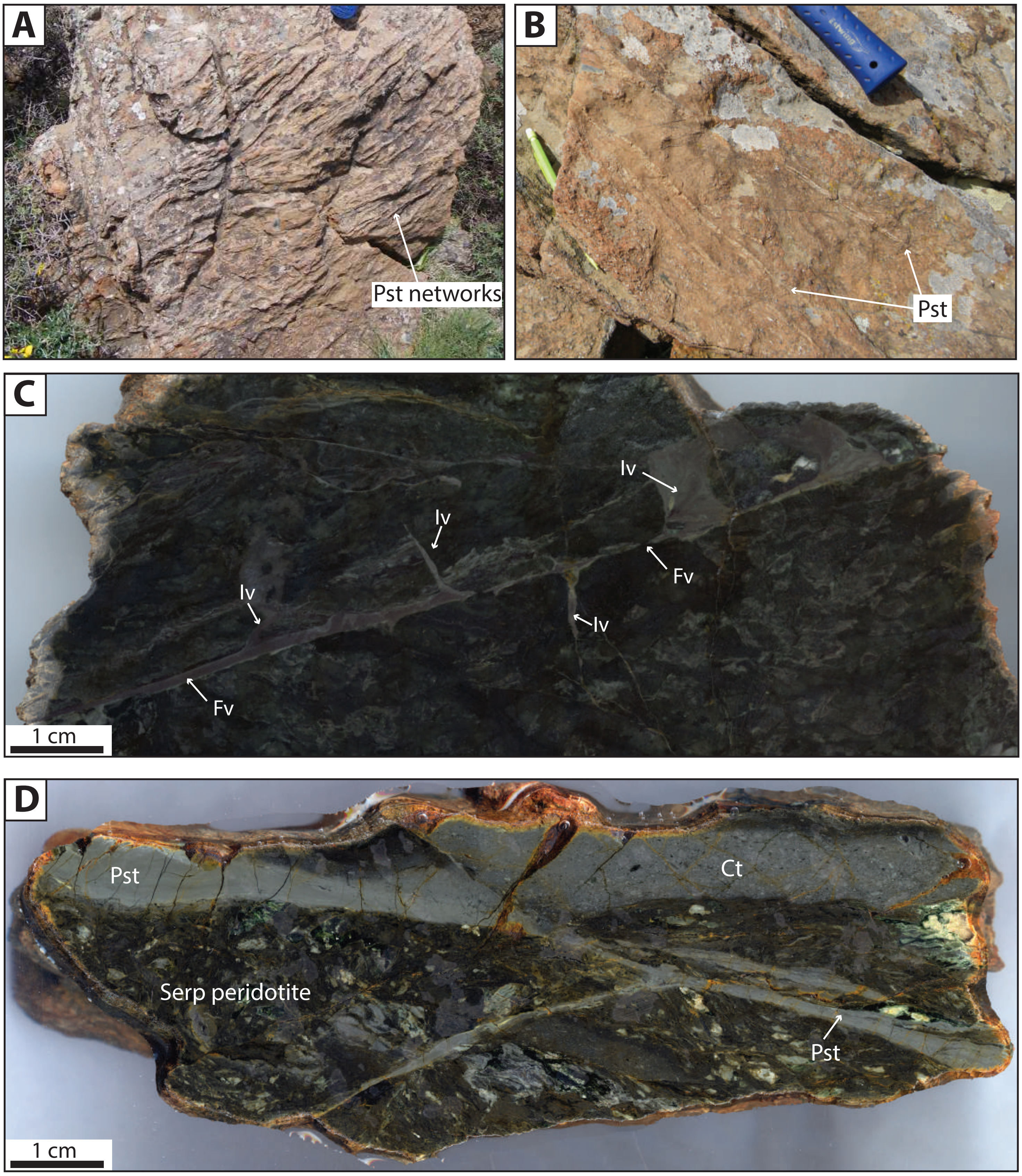
A
Pst networks
B
Pst
C
Iv
Iv
Iv
Fv
Iv
Fv
1 cm
D
Pst
Ct
Serp peridotite
Pst
1 cm

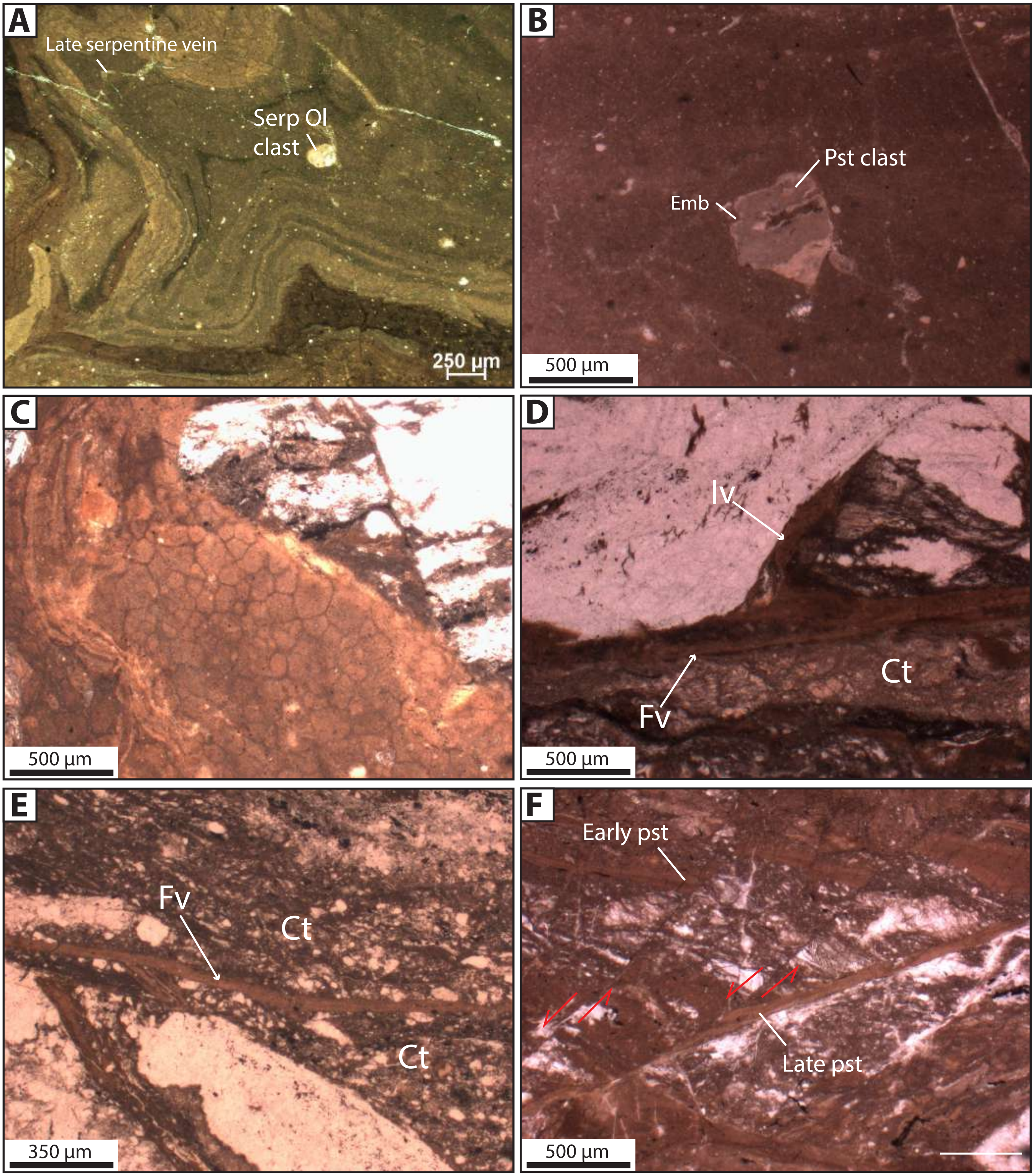
A
Late serpentine vein
Serp Ol clast
250 µm
B
Pst clast
Emb
500 µm
C
500 µm
D
Iv
Fv
Ct
500 µm
E
Fv
Ct
Ct
350 µm
F
Early pst
Late pst
500 µm

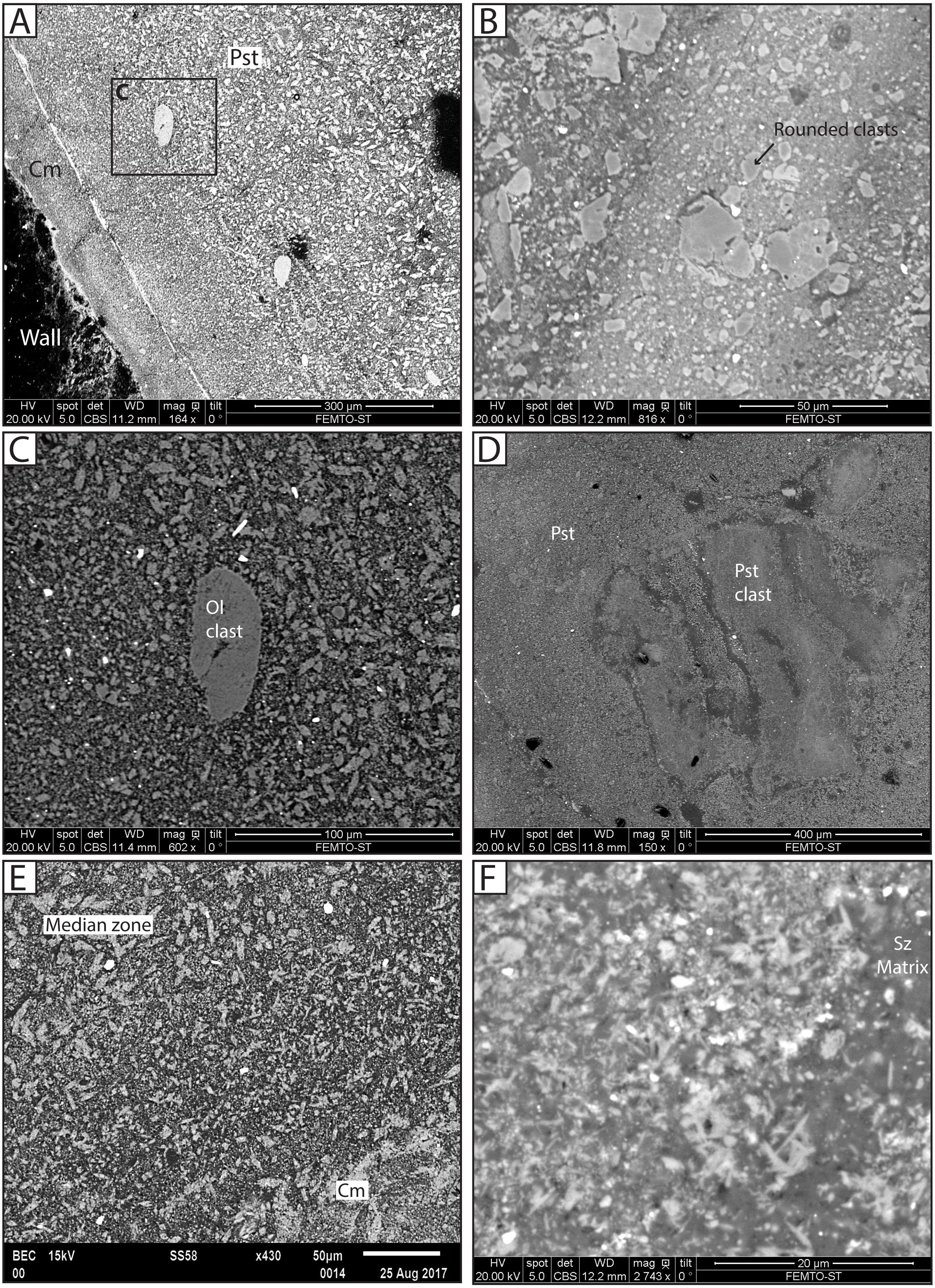
A
Pst
C
Cm
Wall
HV 20.00 kV spot 5.0 det CBS WD 11.2 mm mag 164 x tilt 0 °
300 µm
FEMTO-ST
B
Rounded clasts
HV 20.00 kV spot 5.0 det CBS WD 12.2 mm mag 816 x tilt 0 °
50 µm
FEMTO-ST
C
Ol
clast
HV 20.00 kV spot 5.0 det CBS WD 11.4 mm mag 602 x tilt 0 °
100 µm
FEMTO-ST
D
Pst
Pst
clast
HV 20.00 kV spot 5.0 det CBS WD 11.8 mm mag 150 x tilt 0 °
400 µm
FEMTO-ST
E
Median zone
Cm
BEC 15kV SS58 x430 50µm
00 0014 25 Aug 2017
F
Sz
Matrix
HV 20.00 kV spot 5.0 det CBS WD 12.2 mm mag 2 743 x tilt 0 °
20 µm
FEMTO-ST

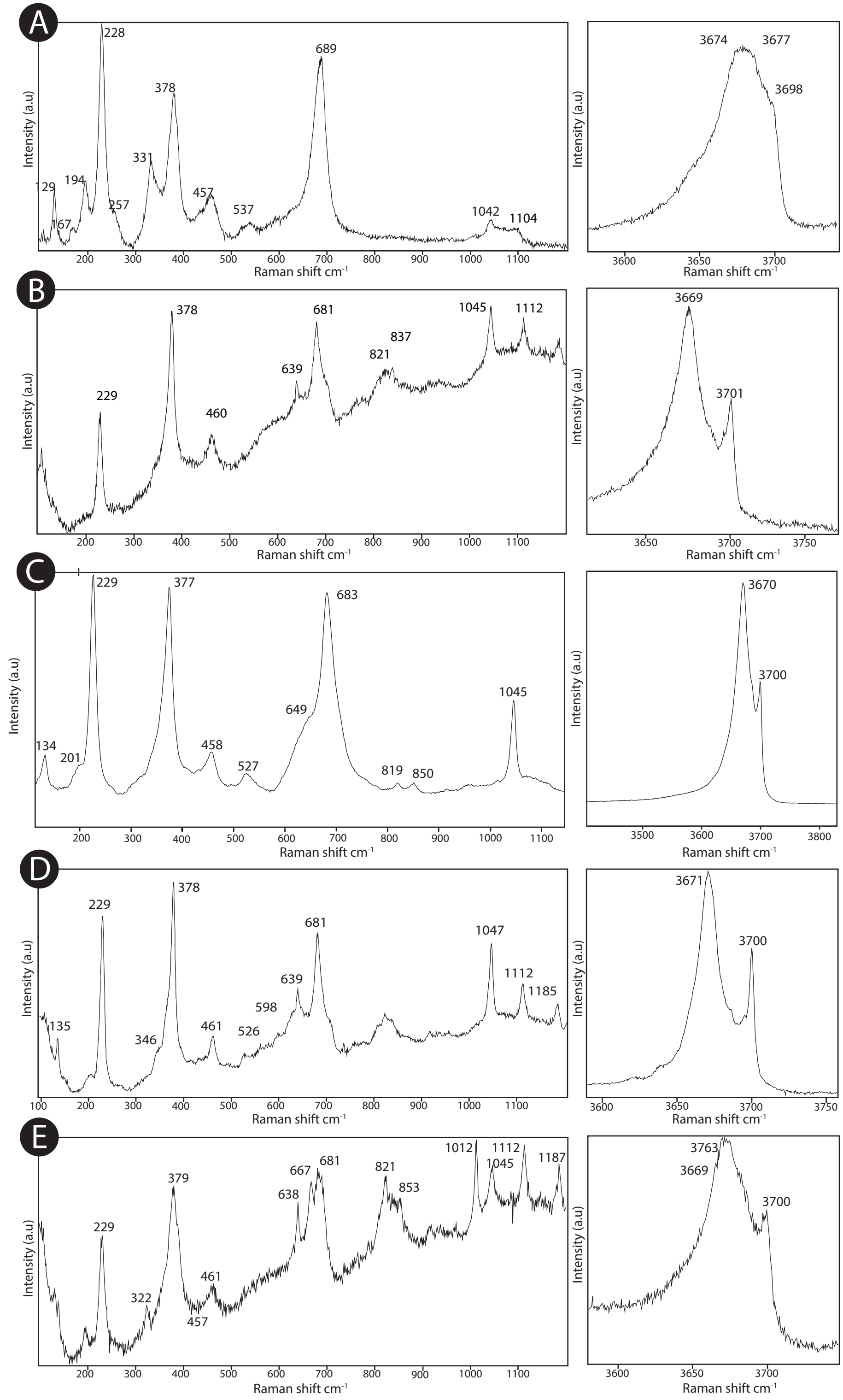
A
129
167
194
228
257
331
378
457
537
689
1042
1104
3674
3677
3698
B
229
378
460
639
681
821
837
1045
1112
3669
3701
C
134
201
229
377
458
527
649
683
819
850
1045
3670
3700
D
135
229
346
378
461
526
598
639
681
1047
1112
1185
3671
3700
E
229
322
379
457
461
638
667
681
821
853
1012
1045
1112
1187
3669
3763
3700
Intensity (a.u)
Raman shift cm-1

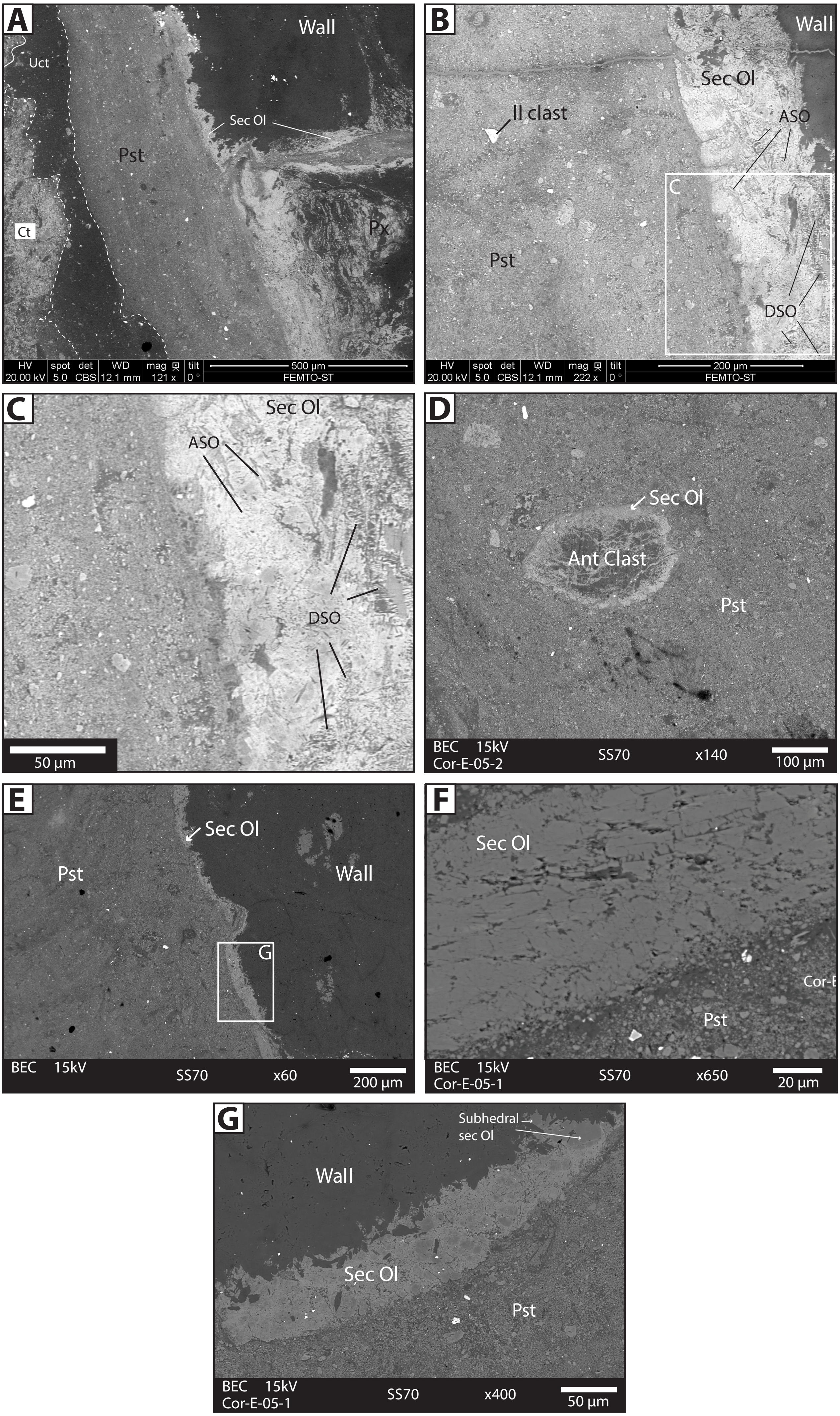
A
Wall
Uct
Sec Ol
Pst
Ct
Px
HV 20.00 kV
spot 5.0
det CBS
WD 12.1 mm
mag 121 x
tilt 0 °
500 µm
FEMTO-ST
B
Wall
Sec Ol
Il clast
ASO
C
Pst
DSO
HV 20.00 kV
spot 5.0
det CBS
WD 12.1 mm
mag 222 x
tilt 0 °
200 µm
FEMTO-ST
C
Sec Ol
ASO
DSO
50 µm
D
Sec Ol
Ant Clast
Pst
BEC 15kV
Cor-E-05-2
SS70
x140
100 µm
E
Sec Ol
Pst
Wall
G
BEC 15kV
SS70
x60
200 µm
F
Sec Ol
Cor-E
Pst
BEC 15kV
Cor-E-05-1
SS70
x650
20 µm
G
Subhedral sec Ol
Wall
Sec Ol
Pst
BEC 15kV
Cor-E-05-1
SS70
x400
50 µm

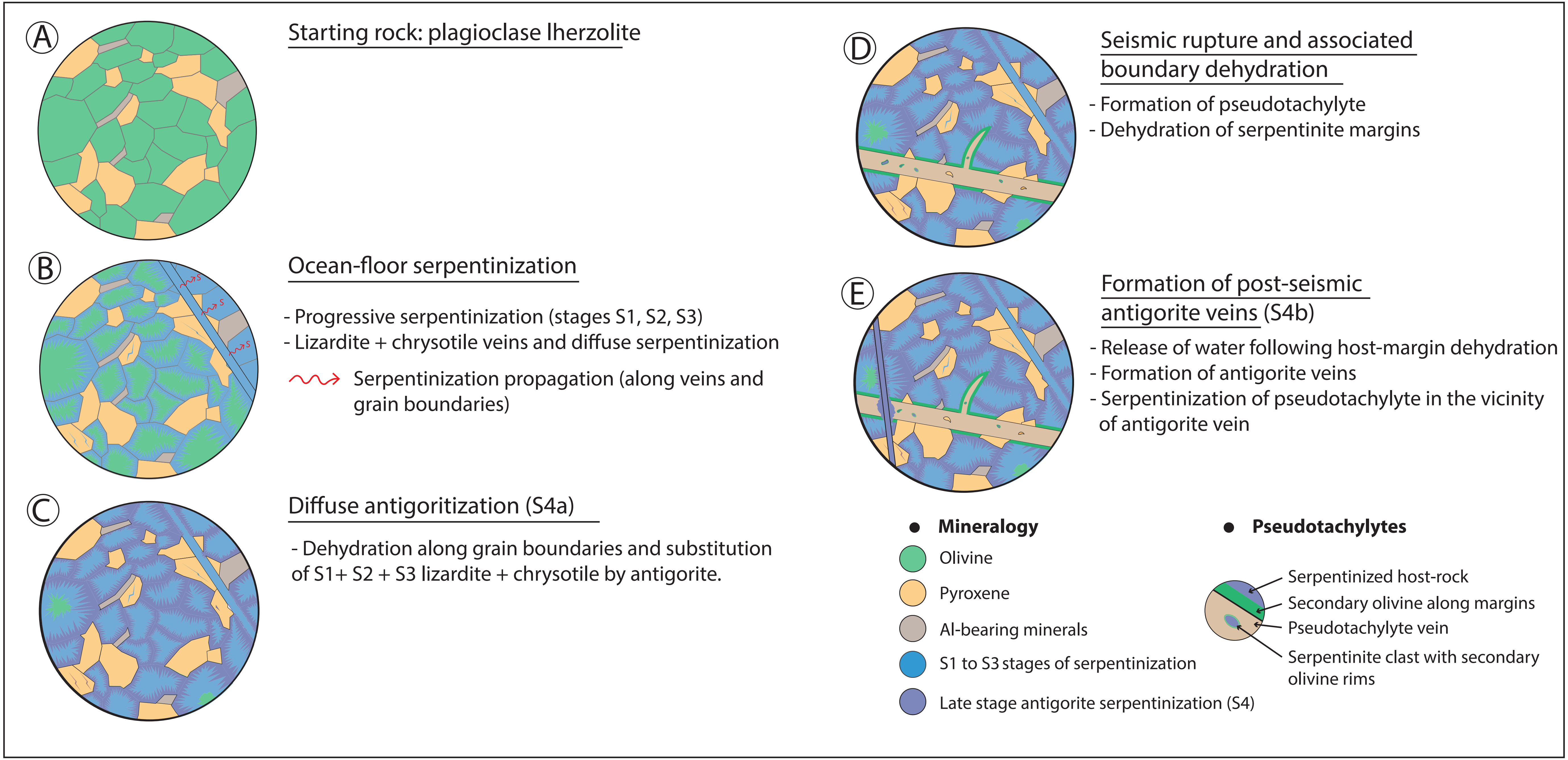

A. Starting rock: plagioclase lherzolite

B. Ocean-floor serpentinization

- Progressive serpentinization (stages S1, S2, S3)
- Lizardite + chrysotile veins and diffuse serpentinization

⇝ Serpentinization propagation (along veins and grain boundaries)

C. Diffuse antigoritization (S4a)

- Dehydration along grain boundaries and substitution of S1+ S2 + S3 lizardite + chrysotile by antigorite.

D. Seismic rupture and associated boundary dehydration

- Formation of pseudotachylyte
- Dehydration of serpentinite margins

E. Formation of post-seismic antigorite veins (S4b)

- Release of water following host-margin dehydration
- Formation of antigorite veins
- Serpentinization of pseudotachylyte in the vicinity of antigorite vein

- **Mineralogy**
  - Olivine
  - Pyroxene
  - Al-bearing minerals
  - S1 to S3 stages of serpentinization
  - Late stage antigorite serpentinization (S4)

- **Pseudotachylytes**
  - Serpentinized host-rock
  - Secondary olivine along margins
  - Pseudotachylyte vein
  - Serpentinite clast with secondary olivine rims

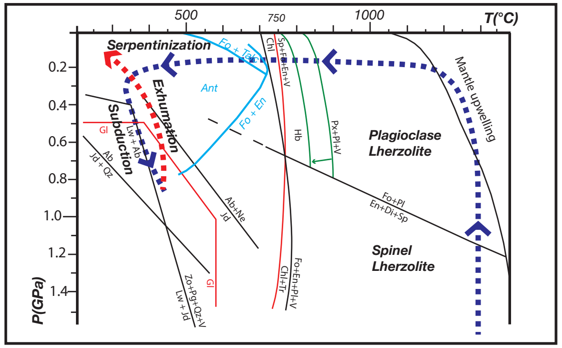
500
750
1000
T(°C)
0.2
0.4
0.6
0.8
1.0
1.2
1.4
P(GPa)
Serpentinization
Fo + Talc
Chl
Sp+Fo+En+V
Mantle upwelling
Ant
Exhumation
Subduction
Fo + En
Gl
Lw + Ab
Ab
Jd + Qz
Hb
Px+Pl+V
Plagioclase
Lherzolite
Fo+Pl
En+Di+Sp
Ab+Ne
Jd
Spinel
Lherzolite
Gl
Zo+Pg+Qz+V
Lw + Jd
Chl+Tr
Fo+En+Pl+V

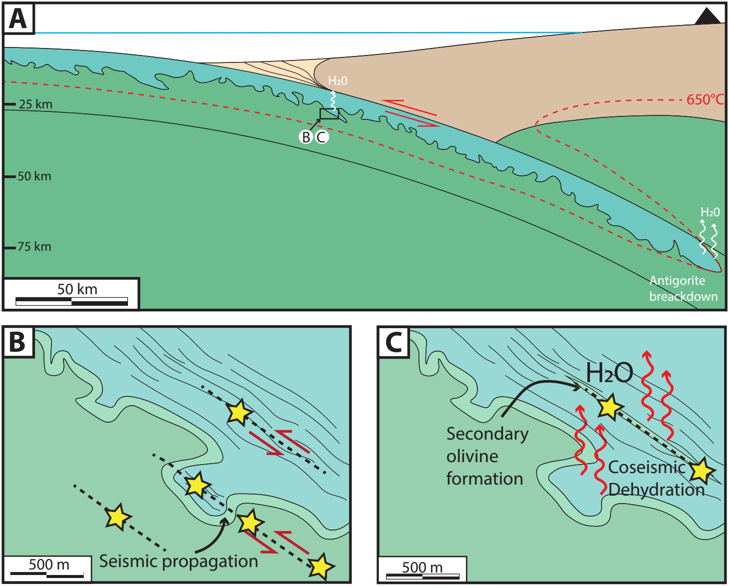
A
H_20
650°C
25 km
B C
50 km
75 km
H_20
50 km
Antigorite
breackdown
B
500 m
Seismic propagation
C
H_2O
Secondary
olivine
formation
Coseismic
Dehydration
500 m

Host-rock and Dehydrated border

wt.% analysis	Border Olivine	Border Olivine	Border Olivine (dark)	Border Olivine (light)	US Host rock Olivine	US Host rock Olivine	US Host rock Opx	US Host rock Cpx	SZ Host rock Serp-Ant	SZ Host rock Serp-Ant
SiO2	39.28	38.45	41.23	39.88	40.95	40.65	54.84	54.86	44.36	44.22
MgO	41.26	37.6	43.38	39.45	50.85	49.95	32.68	23.41	39.88	39.38
FeO	18.69	23.51	14.4	21.75	10.64	9.27	6.01	4.04	4.55	4.85
Al2O3	0.23	0.1	0	0.23	0	0.17	4.03	5.42	0.82	0.65
Na2O	0	0	0	0	0	0	0.03	0.39	0	0.02
CaO	0	0	0	0	0	0.09	1.31	12.33	0.03	0
K2O	0	0	0	0	0	0	0	0	0.02	0.01
MnO	0.57	1	0.8	0	0.24	0	0.11	0.02	0.05	0.06
TiO2	0	0	0	0.12	0	0	0.06	0.18	0.04	0.02
Cr2O3	0	0	0	0	0	0.04	0.61	0	0.02	0
NiO	0.12	0.17	0.11	0.22	0.38	0	0	0.03	0.17	0.07
Total	100.15	100.83	99.92	101.65	103.06	100.17	99.68	100.68	89.94	89.28
Mg #	68.82	61.53	74.05	64.46	82.37	84.35			89.66	88.91

Pseudotachylytes

wt.% analysis	Microlite Cpx	Microlite Cpx	Microlite Cpx	Matrix	Matrix	Clast Cpx	Clast Ol	Clast Serp-Ol	Clast Ilmenite
SiO2	52	49.77	51.52	40.11	39.48	52.15	40.84	40.08	2.51
MgO	17.35	26.97	17.3	32.37	34.31	13.42	51.01	40.8	2.86
FeO	7.03	3.17	6.55	8.69	12.23	10.59	10.65	8.22	39.87
Al2O3	1.37	3.5	2.46	6.52	5.72	0.84	0	2.15	0.78
Na2O	0	0.58	0.24	0.11	0	0.18	0	0	0
CaO	22.42	11.73	21.17	3.76	2.91	23.43	0	0.1	0
K2O	0.02	0	0	0	0	0	0	0	0
MnO	0	0.13	0	0.2	0.39	0.3	0.21	0.17	2.9
TiO2	0	0.16	0.26	0.31	0.23	0	0	0.08	51.33
Cr2O3	0.1	0.17	0	0.29	0.15	0	0	0.1	0
NiO	0.15	0	0.21	0.12	0.08	0	0.32	0.08	0
Total	100.44	96.18	99.71	92.48	95.5	100.91	103.05	91.77	100.25
% Fo	/	/	/	/	/		82.40	82.94	/